Title	The Energy-resolved neutron imaging system, RADEN
Author(s)	Shinohara Takenao, Kai Tetsuya, Oikawa Kenichi, Nakatani Takeshi, Segawa Mariko, Hiroi Kosuke, Su Y., Oi Motoki, Harada Masahide, Iikura Hiroshi, Hayashida Hirotoshi, Parker J. D., Matsumoto Yoshihiro, Kamiyama Takashi, Sato Hirotaka, Kiyanagi Yoshiaki
Citation	Review of Scientific Instruments,91(4), p.043302_1-043302_20
Text Version	Published Journal Article
URL	https://jopss.jaea.go.jp/search/servlet/search?5068711
DOI	https://doi.org/10.1063/1.5136034
Right	

Review of Scientific Instruments ARTICLE scitation.org/journal/rsi

The energy-resolved neutron imaging system, RADEN

Cite as: Rev. Sci. Instrum. 91, 043302 (2020); doi: 10.1063/1.5136034
Submitted: 10 November 2019 • Accepted: 14 March 2020 •
Published Online: 2 April 2020

Takenao Shinohara,[1,a)] Tetsuya Kai,[1] Kenichi Oikawa,[1] Takeshi Nakatani,[1] Mariko Segawa,[1] Kosuke Hiroi,[1] Yuhua Su,[1] Motoki Ooi,[1] Masahide Harada,[1] Hiroshi Iikura,[1] Hirotoshi Hayashida,[2] Joseph D. Parker,[2] Yoshihiro Matsumoto,[2] Takashi Kamiyama,[3] Hirotaka Sato,[3] and Yoshiaki Kiyanagi[3,4]

AFFILIATIONS

[1]J-PARC Center, Japan Atomic Energy Agency, Tokai, Ibaraki 319-1195, Japan
[2]Neutron Science and Technology Center, Comprehensive Research Organization for Science and Society, Tokai, Ibaraki 319-1106, Japan
[3]Faculty of Engineering, Hokkaido University, Sapporo, Hokkaido 060-8628, Japan
[4]Graduate School of Engineering, Nagoya University, Nagoya, Aichi 464-8601, Japan

[a)]**Author to whom correspondence should be addressed:** takenao.shinohara@j-parc.jp

ABSTRACT

The energy-resolved neutron imaging system, RADEN, has been installed at the pulsed neutron source in the Materials and Life Science Experimental Facility of the Japan Proton Accelerator Research Complex. In addition to conventional neutron radiography and tomography, RADEN, the world's first imaging beam-line at a pulsed neutron source, provides three main options for new, quantitative neutron imaging techniques: Bragg-edge imaging to visualize the spatial distribution of crystallographic information, resonance absorption imaging for elemental composition and temperature information, and polarized neutron imaging for magnetic field information. This paper describes the results of characterization studies of the neutronic performance and installed devices at RADEN and shows the results of several demonstration studies for pulsed neutron imaging.

I. INTRODUCTION

Neutron imaging is a fundamental technique for visualizing the internal structure of objects and is regarded as an indispensable tool for non-destructive inspection due to its high penetration into materials and sensitivity to light elements such as hydrogen, lithium, and boron. Neutron imaging is utilized in a variety of fields in not only academia but also industry. Recent progress in neutron imaging instruments and development of related devices has allowed the establishment of new neutron imaging techniques. Consequently, neutron imaging has come into a new stage; that is, it is not merely a non-destructive method for inspection of internal shapes or structures, but a multi-dimensional measurement of physical/chemical properties of objects. In particular, the neutron imaging techniques that analyze neutron wavelength or energy dependence of transmission spectra position by position,[1,2] referred to collectively as energy-resolved neutron imaging, enable us to quantitatively visualize, for example, crystallographic information using Bragg-edge imaging,[3–6] or composition or temperature distributions using neutron resonance absorption imaging.[7–10] Moreover, this technique brings about the capability of quantitative magnetic field imaging in combination with neutron polarization analysis[11–13] and small-angle neutron scattering (SANS) information by the introduction of the grating interferometer.[14–18] Here, the short-pulsed neutron sources have a big advantage for conducting energy-resolved neutron imaging efficiently and precisely compared with steady neutron sources due to the following reasons: it is possible to determine the neutron energy/wavelength by means of the Time-of-Flight (ToF) method, the intrinsically narrow pulse structure provides fine energy/wavelength resolutions of less than 1%, and the wide available energy range, from several keV down to meV, allows Bragg-edge imaging and neutron resonance absorption imaging to

be performed simultaneously. These unique features of the pulsed neutron beam cannot be achieved by the wavelength/energy selection imaging techniques conducted at reactor-based neutron sources and enable the quantification of many physical or elemental properties by means of precise spectral analysis. Until recently, the low intensity of the pulsed neutron beams has been a limiting factor for the application of these imaging techniques, but the situation has changed owing to the construction of new imaging instruments at high-power spallation neutron sources such as Japan Proton Accelerator Research Complex (J-PARC),[19,20] ISIS,[21] Spallation Neutron Source (SNS),[22] and the future European Spallation Source (ESS).[23]

Of these new imaging instruments, the Energy-Resolved Neutron Imaging System "RADEN," formerly named ERNIS, at the Materials and Life Science Experimental Facility (MLF) of J-PARC started construction in 2012 after intensive development studies using the pulsed neutron facilities at Hokkaido University (HUNS)[24] and the NOBORU instrument at the J-PARC MLF.[25] RADEN then launched its operation in November 2014 as the world's first dedicated instrument to neutron imaging using pulsed neutrons. The most important purpose of the RADEN instrument is to provide the most suitable experimental environment for energy-resolved neutron imaging and to promote practical application studies using these techniques. In addition, RADEN is equipped for conventional neutron radiography and tomography measurements, where the white neutron beam is used to obtain transmission images, representing the state-of-the-art neutron imaging facility with sufficient neutron flux in Japan. In this paper, we discuss the neutronic performance of the RADEN instrument and present results of demonstration studies conducted at RADEN.

II. OUTLINE OF THE RADEN INSTRUMENT

Before entering the main subject, we briefly introduce the outline of the RADEN instrument. An illustration of RADEN is shown in Fig. 1, and its basic parameters are summarized in Table I. RADEN is installed at beamline number 22 (BL-22) in the MLF and views the decoupled hydrogen moderator. The instrument structure is roughly divided into two sections: an upstream optics section and a downstream experimental area. In the upstream optics section, devices for beam collimation and shaping, consisting of a heavy shutter, two rotary collimators, and beam slits, are installed to provide various L/D values (here, D is the width of an aperture and L is the distance from the aperture to the detector) and an appropriate beam size for a given sample. There are also devices for energy selection, such as filters, a double-disk chopper, and a T0 chopper, to define the available wavelength range and to eliminate background due to the prompt neutron pulse and accompanying flash γ-rays. In addition, a light shutter, referred to as a blocker, is included to reduce undesired sample activation. The details of the RADEN instrument design are described in Ref. 20. In the experimental area, RADEN features two sample positions: one at 18 m (near sample position) and the other at 23 m (far sample position) from the source. The near sample position can cover a broad wavelength range in one neutron-pulse frame, which is 40 ms in J-PARC, while the far position provides a wide field-of-view (FoV) and a finer wavelength/energy resolution. A flight-tube exchange lift is placed in front of the near sample position, which is used to exchange a flight tube filled with He gas with a neutron polarization apparatus, so as to easily switch the setup from an unpolarized to a polarized neutron beam. RADEN is equipped with three stages to mount and position samples and sample environments. A large sample stage placed at the far sample position can mount samples up to 1-ton in weight and provides for remote translation and rotation of the sample. A medium-sized stage, with a capacity up to 600 kg, is placed at the near sample position, and a small stage is available for use in combination with the medium and large stages. The specifications of these stages are described in Table II. Additionally, several small rotary and linear motion stages are available for computed tomography (CT) measurements and automatic sample exchange.

In Secs. III–VI, we describe in detail the neutron beam performance, detectors, and software for both controlling devices and performing data analysis, and finally, we show the results of several demonstration studies for energy-resolved and conventional neutron imaging techniques.

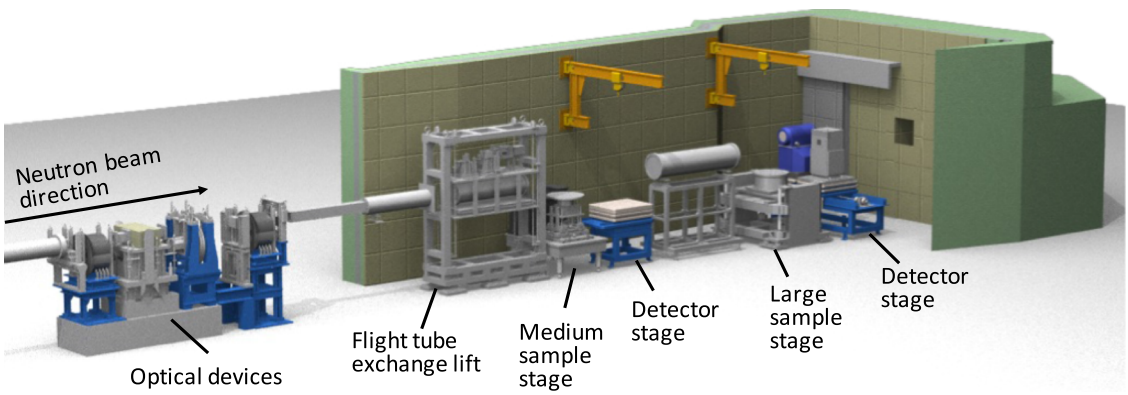

FIG. 1. Illustration of the RADEN instrument.

TABLE I. Summary of the basic parameters of the RADEN instrument.

Beam line number	BL-22
Moderator type	Decoupled hydrogen moderator
Available wavelength (energy) range	$\lambda < 8.8$ Å ($E > 1.1$ meV)
Wavelength resolution	$\Delta\lambda/\lambda > 0.2\%$ ($\lambda > 3$ Å, $L_S = 23$ m)
Neutron beam intensity (@1 MW)	1.7×10^7 n/s/cm^2 ($E < 0.45$ eV, $L/D = 180$) 1.1×10^8 n/s/cm^2 ($E < 1$ MeV, $L/D = 180$) 3.9×10^6 n/s/cm^2/eV ($E = 1$ eV, $L/D = 180$)
Source–sample distance	$L_S = 18$ m, 23 m
Maximum field-of-view (FoV)	300×300 mm^2 (see Table III)
Available L/D value (designed)	180–7500 (see Table III)
Imaging detector systems	Counting type (μNID, nGEM, LiTA) (see Table IV) Camera-type (^{6}LiF + ZnS scintillator + CCD, EM-CCD, sCMOS)
Spatial resolution	>100 μm (counting-type detectors) >30 μm (CCD camera-type detectors)
Available sample environments and optional detector systems	Sample stages (see Table II) ToF polarimetry apparatus Sample heaters (infrared heating, electric heating) Diffraction detector (^{3}He 1D-PSDs), γ-ray detector

TABLE II. Specifications of the sample stages available at RADEN. Here the *x*, *y*, and *z* axes are taken along horizontal, vertical, and neutron beam directions, respectively.

Stage name	Position	Movable axis			Maximum load	Table size
		θ (deg)	x, y, z (mm)	R_x, R_y (deg)		
Large	$L_S = 23$ m	±173	±300	...	1.0 ton	ϕ 700 mm, 750 mm-sq
Medium	$L_S = 18$ m	±173	±100	±5	600 kg	ϕ 300 mm, 750 mm-sq
Small	Portable	±180	...	±5	10 kg	ϕ 150 mm

III. NEUTRON BEAM PERFORMANCE

A. Neutron intensity and spectrum

The neutron flux intensity at RADEN was measured by the gold foil activation method. A pair of $15 \times 15 \times 0.05$ mm^3 gold foils were placed at the end of the neutron flight tube at the upstream side of the experimental area ($L_S = 14.4$ m), where L_S is the distance from the source, and were irradiated by neutrons with and without a 1-mm thick cadmium filter for 10 min at a proton beam power of 200 kW. For these measurements, the upstream optics were adjusted to provide an L/D of 180, which is the highest intensity setting available at RADEN. The effective activation cross section was calculated as 131 barns using the evaluated nuclear data library JENDL-4[26] and the measured spectrum mentioned below. The γ-rays from ^{198}Au, which was produced by activation of ^{197}Au, were measured with a high-purity germanium detector, and the neutron flux below the cadmium cutoff energy of 0.45 eV was determined to be 2.6×10^7 n/s/cm^2/MW (at the $L_S = 14.4$ m position) with an experimental error of 20%. This corresponds to a flux of 1.7×10^7 n/s/cm^2/MW at the near sample position (for $L/D = 180$).

The neutron spectrum was measured with a ^{3}He proportional counter located at $L_S = 15.5$ m. The efficiency was 10^{-5} at 25 meV and was assumed to be inversely proportional to the square root of the neutron energy. Figure 2 shows the measured spectra

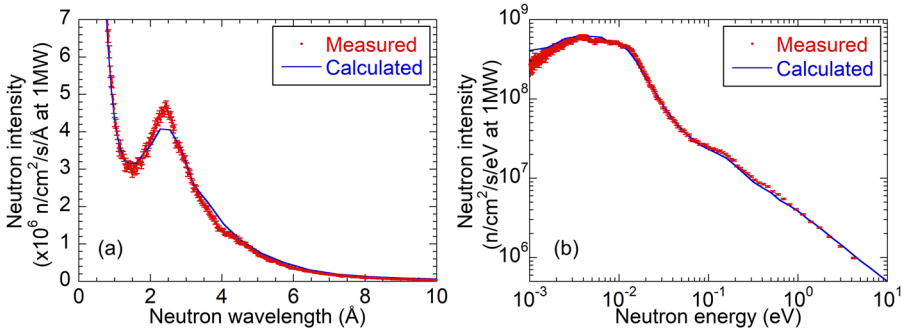

FIG. 2. Comparison of measured and calculated neutron energy spectra as a function of neutron wavelength (a) and energy (b) normalized by the neutron intensity measured by the gold foil activation method. Error bars indicate statistical uncertainties of the spectrum measurement.

as functions of neutron wavelength (a) and energy (b). The absolute values were normalized by the neutron intensity derived from the gold foil activation method, giving an integrated intensity below 1 MeV of 1.1×10^8 n/s/cm^2/MW and an intensity at 1 eV of 3.9×10^6 n/s/cm^2/eV/MW. The measured neutron intensity agreed with the value calculated during the design of RADEN[20] within experimental errors. The calculated spectra, being normalized in the same manner as the measured ones, agreed well in overall shape, as shown in Fig. 2.

B. Pulse shapes

The pulse shapes of the thermal and cold neutrons, with E_n from around 100 meV and lower, were measured by a conventional diffraction method, where the sample and experimental setup were almost the same as previous work done at the NOBORU instrument of J-PARC.[27] The plate-like sample, *c*-axis aligned crystal mica, was set on a small goniometer mounted on the large sample stage. The reason why a crystal mica was chosen as the monochromator to evaluate the incident neutron beam's pulse shape is that this crystal has a large lattice spacing and small diffuse scattering and does not show line broadening due to the crystalline size and/or microstrain. A zero-dimensional 1/2-in. ^{3}He gas proportional counter was set 1.2 m from the sample at an angle of $2\theta = 170^\circ$, where θ denotes the Bragg angle of the sample, and the measurement was carried out with a beam power of 500 kW. Figure 3 shows an example of pulse shapes for the thermal and cold neutrons. Bragg peaks of (008) and (0036) of mica are plotted in linear scale [Figs. 3(a) and 3(c)] and semi-log scale [Figs. 3(b) and 3(d)]. The observed Bragg peaks are plotted as open circles on a solid line (obs.), and the corresponding peaks simulated by the McStas code[28] are plotted as filled circles on a dashed line (sim.). For the simulation, the main instrument components, such as the steel collimator, beam slit, sample, and detector, were modeled in the instrument file of the McStas code, and the pulse structure data of BL-22 in the MLF calculated by the Particle and Heavy Ion Transport code System (PHITS) simulation code[29] were included as a table in the source component of the McStas code. In this simulation, the crystal mica was considered as a perfect crystal, and the geometrical contribution to the measured pulse shape was seen to be sufficiently small in this experimental arrangement with, at most, only a 3% increase in full width at half maximum (FWHM). Hence, the simulated Bragg peak shape can be mostly attributed to the incident beam's pulse shape. The measured pulse shapes agreed well with the ones simulated using the McStas code, as shown in Fig. 3. The obtained FWHM values of each Bragg peak are summarized in Fig. 4. The observed FWHM of pulse shapes for the thermal and cold neutrons showed good agreement with the simulation results with the PHITS code, supporting our instrument design for the wavelength resolution required for Bragg-edge imaging.[30]

C. Beam size and divergence

RADEN has seven apertures to control the beam size and beam divergence (indicated by L/D) located in the heavy shutter and two

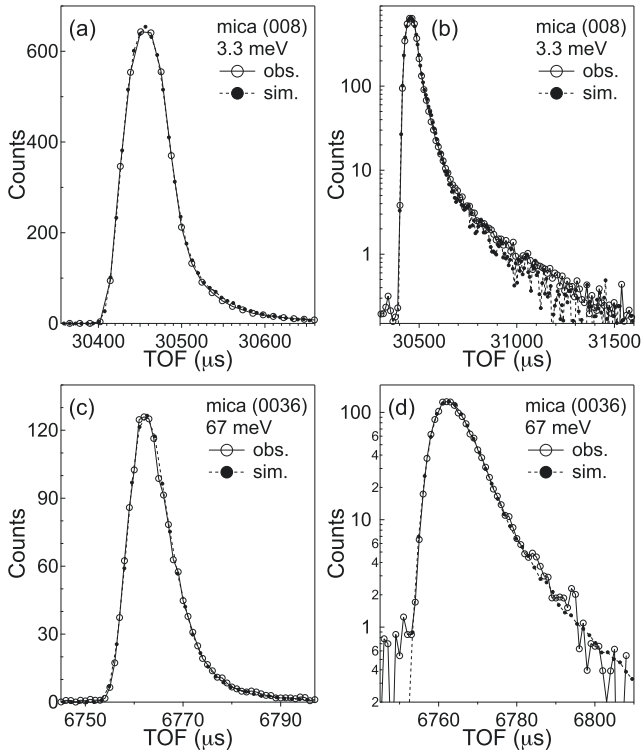

FIG. 3. Examples of pulse shapes for cold and thermal neutrons. Bragg peaks of (008) and (0036) of mica are represented in linear [(a) and (c)] and log [(b) and (d)] scale. The measured FWHM of the observed Bragg peaks of (008) and (0036) is 64 μs and 9.8 μs, respectively, which correspond to the time-distributions of the incident neutron beam's pulse width.

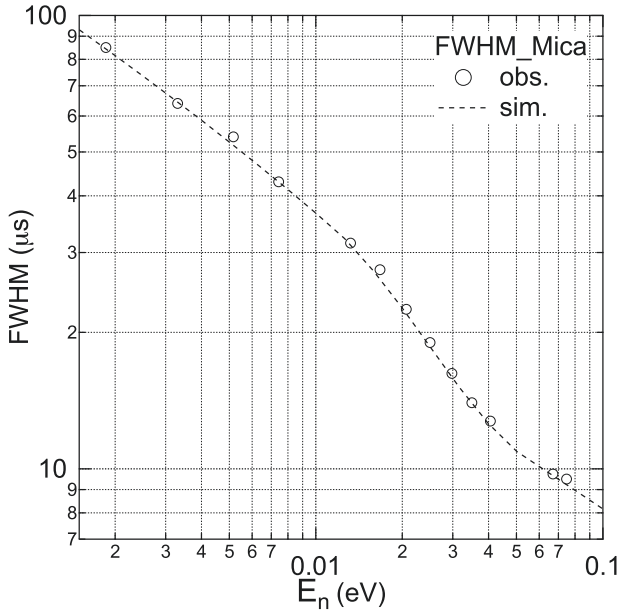

FIG. 4. Energy dependence of FWHM for observed Bragg peaks (open circles). The intrinsic FWHM of the incident neutron's pulse shape simulated by the PHITS code is overlaid (dashed line).

rotary collimators (RC-1 and RC-2).[20] In the shutter, three apertures with sizes of 100 × 100 mm^2, ϕ 50.1 mm, and ϕ 26.4 mm are installed.[31] Another three apertures of size ϕ 15 mm, ϕ 5 mm, and ϕ 2 mm are installed in RC-1, and an aperture of ϕ 6 mm is installed in RC-2. The beam size and L/D values for each aperture were measured using a camera-type detector (consisting of a ^{6}LiF + ZnS scintillator with a thickness of 100 μm and a back-illuminated CCD camera) placed at the far sample position. The parameters obtained for each aperture are listed in Table III.

The beam size was defined as the size of the flat region around the center of the beam profile. To illustrate this, the result of the beam size measurement for the 100 × 100 mm^2 aperture is shown in Fig. 5, consisting of the obtained two-dimensional image and its one-dimensional profiles along the horizontal and vertical directions. Differential beam profiles are also shown in Figs. 5(b) and 5(c) as red lines. The limits of the flat region were determined by looking for abrupt changes in the differential profile. The measured beam sizes, shown in Table III, were in good agreement with, although slightly larger than, the design values. The largest beam size, however, was not exactly characterized, since the scintillator used for the measurement had a size of 300 × 300 mm^2 or the same as the expected beam size. Because the beam intensity profile was smooth and no kinks were seen in the profile, we concluded that the largest beam size was at least the same or larger than the design value. In addition to the measured beam size, the relative neutron flux for each aperture, calculated as the ratio of the observed neutron intensity integrated over a 100 × 100 mm^2 area around the beam center relative to that for the 100 mm-sq. aperture case, is listed in Table III.

The effective L/D value of each aperture was evaluated using a Gd thin-film test target,[32] which was placed at multiple separations, l, from the detector [Fig. 6(a)]. A ^{6}LiF + ZnS scintillator screen with a thickness of 50 μm and a back-illuminated CCD camera were used as the imaging detector. From the intensity profile at the edge of the Gd test target image, the corresponding edge-spread and line-spread functions were obtained. Figure 6(b) shows typical results obtained from the Gd test target placed at l = 300 mm and l = 700 mm for the ϕ 50.1 mm aperture. To determine the L/D values for each aperture, the geometric blurring, d, was first evaluated as the standard deviation value, 2σ, by fitting the line-spread functions for each l with a Gaussian function. Here, the contribution from Fresnel diffraction by the edge of the Gd pattern to the blurring of the profile was calculated to be negligibly small. The resulting L/D values were then determined as the slope of a linear fit to the distributions of d as a function of l [Fig. 6(c)]. Overall, the obtained L/D values were consistent with the designed L/D values as shown in Table III, although the measured values at higher L/D were slightly smaller than the designed values. Since the evaluation of the high L/D values required a longer distance between the sample and detector compared to the low L/D values, the edge-spread function is thought to have been broadened by neutron scattering in air, leading to the reduced L/D.

D. T0 and double-disk choppers

The high-energy neutrons and γ-rays produced at the time of proton-beam pulse injection on the target cause an increase in background and can damage the electric devices in the experimental area. A T0 chopper was installed at the distance of 8.7 m from the neutron source to mitigate such effects by bringing a rotating

TABLE III. L/D and beam size of RADEN at the far sample position (L_S = 23 m). Beam size is written as horizontal × vertical length in mm. The beam size with the aperture of ϕ 26.4 mm could not be characterized by the measurement using the 300 × 300 mm^2 scintillator.

Aperture size	100 mm-sq	ϕ 50.1 mm	ϕ 26.4 mm	ϕ 15 mm	ϕ 6 mm	ϕ 5 mm	ϕ 2 mm
Aperture position from the source (m)	...	3.1	4.3	8.0	11.15	8.0	8.0
L/D (designed)	230	398	720	1000	1975	3000	7500
L/D (measured)	250	420	760	1090	2030	2970	7370
Beam size (designed) (mm^2)	100 × 100	250 × 250	300 × 300	144 × 144	100 × 100	173 × 173	181 × 181
Beam size (measured) (mm^2)	104 × 104	255 × 258	...	154 × 155	116 × 103	194 × 189	205 × 196
Relative neutron flux (%)	100	33.7	12.5	4.4	1.0	0.51	0.09

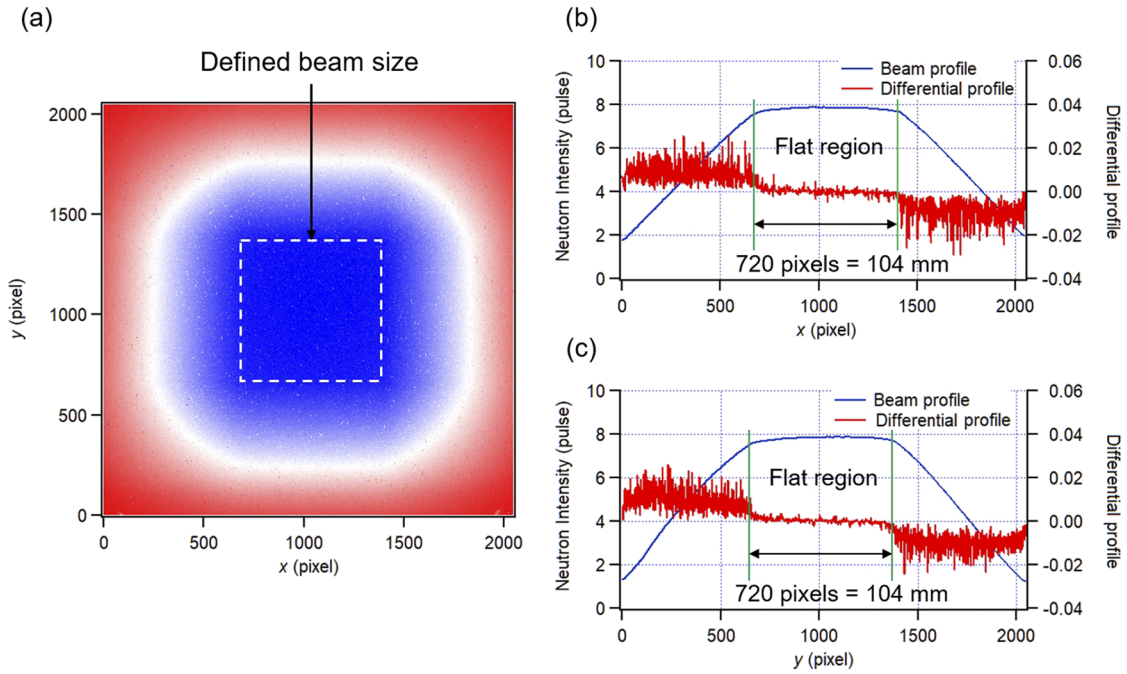

FIG. 5. (a) Results of beam size measurement with an aperture of 100 × 100 mm^2. Beam profiles and differential profiles along the vertical (b) and horizontal (c) directions are also shown.

hammer into the beam at the instant of proton beam injection (T = 0). The rotor, rotating at 25 Hz and synchronized with the accelerator, consists of a hammer made of an Inconel alloy (Inconel X750) having dimensions of 108 × 108 mm^2 in cross section and 300 mm in length and a counterweight made of a stainless steel. Figure 7 shows the neutron count taken with and without rotating the T0 chopper. The spectra were measured with the nGEM detector (described in Sec. IV A 2) placed at L_S = 24 m. The ϕ15 mm aperture of RC-1 and a 25 mm-thick bismuth filter were used, and the double-disk chopper (described below) was used to eliminate pulse-frame overlap. The neutron count with T0 chopper operation was successfully suppressed by more than three orders of magnitude for a neutron time-of-flight up to about 3 ms, while the rapid drop in neutron count after 38 ms was caused by the double-disk chopper. Near the beginning of the pulse, the neutron count increased in the time-of-flight range from 2.7 ms to 3.6 ms (or from 0.41 eV to 0.23 eV in terms of neutron energy) and then returned to the nominal value for the case without T0 chopper operation. This transition region corresponds to the duration for which the hammer edge crosses the collimator hole, which can be understood as follows: At T = 0, the position of the hammer center is at the center of the collimator and the collimator hole was completely covered. The collimator then starts to open at $T = (l_h - d_c)/2v$ and fully opens at $T = (l_h + d_c)/2v$, where l_h is the width of the hammer, d_c is the diameter of the collimator, and v is the velocity of the hammer. When using the largest (102 × 102 mm^2) and smallest (2 mm in diameter) collimator holes of RC-1, the transition ends at 2.2 ms and 1.2 ms, respectively. This means that it is possible to use the neutron beam with energies below 0.080 eV and 0.29 eV, respectively, when the T0 chopper is used.

In addition to the T0 chopper, a double-disk chopper was installed at 9.7 m from the neutron source. This chopper, operating in synchronization with the accelerator, defines the wavelength range of the neutron beam and eliminates contamination of slow neutrons in higher order frames. Each disk was made of an aluminum alloy with an opening angle of 190°, with the remaining 170° coated by a 3 mm-thick $^{10}B_4C$ powder and epoxy resin mixture to absorb neutrons. The phase delay of each disk, θ_d (°), is defined by the position of the leading edge of the disk opening at T = 0, and θ_d = 0° corresponds to the edge positioned at the center of the neutron beam. Then, the disk opens at (40 × θ_d/360) ms and closes at [40 × (θ_d + 190)/360] ms. Thus, the double-disk chopper enables us to select the wavelength range freely with a bandwidth of $\Delta\lambda_{chop}$ in the range 0.9 < $\Delta\lambda_{chop}$ < 8.6 Å in a single frame by independently shifting the opening and closing time of the two disks via their phase delays, θ_d.

An example of neutron beam spectra measured for various θ_d is shown in Fig. 8(a). Here, a ^{3}He neutron counter placed at L_S = 15.1 m was used as the detector. The results clearly indicate that the double-disk chopper efficiently defined the wavelength band and shifted it according to the phase delay. With the smallest relative opening angle of 20°, a neutron beam with wavelength resolution of several 10% is also available [Fig. 8(b)]. This kind of beam setup is beneficial for performing quasi-monochromatic imaging using a camera-type detector without ToF analysis. Figure 8(b) also displays contamination consisting of neutrons coming from higher-order

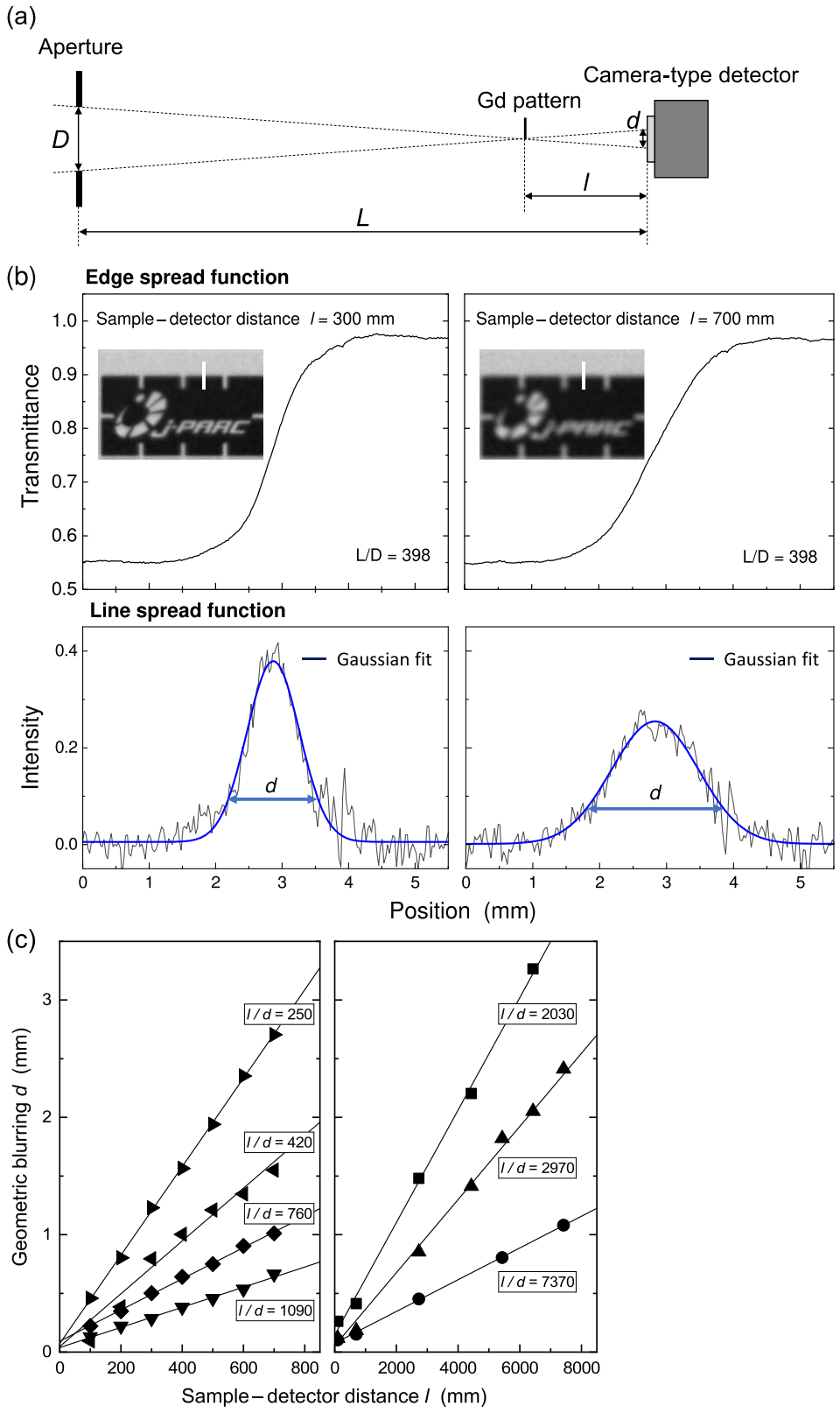

FIG. 6. (a) Schematic diagram of the *L*/*D* measurement. (b) Transmission image, edge-spread functions, and line-spread functions for the edge of the Gd test target obtained at sample–detector distances of *l* = 300 mm and *l* = 700 mm. The white line in the transmission image indicates the position along which the intensity profile was obtained. (c) Geometric blurring, *d*, as a function of sample–detector distance, *l*, with fit results shown as solid lines.

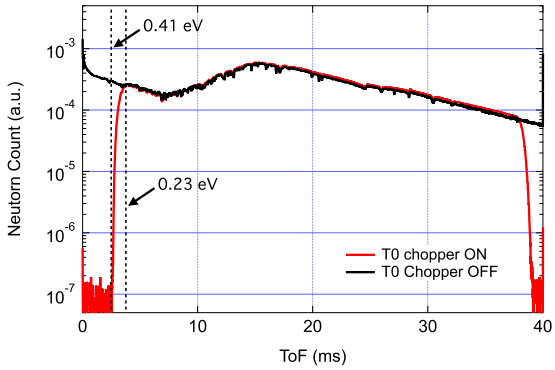

FIG. 7. Neutron count as a function of ToF measured at the 24 m position. Red and black lines indicate neutron count with and without operating the T0 chopper, respectively.

frames but with a neutron count of less than 20. This is because the double-disk chopper stops neutrons in even-order frames but allows neutrons in odd-order frames to pass through. Because the wavelengths of such neutrons are very long, however, the contribution to the overall spectrum is small and can be removed easily by installing a filter.

E. Beam filters

A beam-filter insertion device was installed at 7.4 m from the neutron source in the upstream optics section. These filters are used to tailor the beam characteristics, such as attenuating the neutron beam or tuning the energy distribution, for a given measurement. The insertion device has four linear stages with two filters on each stage, as shown in Fig. 9(a). The dimensions of the filters are 105 × 105 mm^2 to ensure full coverage of the beam, with various thicknesses available to allow tuning for the desired level of filtering. The first stage of the insertion device has a borosilicate glass plate (2 mm in thickness) and an acrylic resin plate (5 mm) for neutron beam attenuation, while the second stage has a cadmium plate (1 mm), used mainly in resonance absorption imaging, and a bismuth (Bi) plate (25 mm). Note that the use of borosilicate glass or the acrylic resin filters is also considered in the case of resonance absorption imaging for elements such as europium (Eu), erbium (Er), iridium (Ir), and some actinide nuclides, having resonances below 1 eV. The third stage has 25 mm thick lead (Pb) and Bi plates, and the fourth has 50 mm thick Pb and Bi plates. The Pb and Bi filters are used to attenuate γ-rays from the neutron source and/or for neutron beam attenuation. Most γ-rays coming from the neutron source, being produced at the moment of proton beam injection, can be effectively reduced by the T0 chopper with an elimination of neutrons above ~0.2 eV. In the case of resonance absorption imaging, the Pb or Bi filters are used instead of the T0 chopper. The filters of each stage can be selected independently; thus, Pb and Bi filters with total thicknesses of 75 mm and 100 mm, respectively, are available by combining filters on two or three stages.

The neutron transmission rates of the filters as a function of energy were measured with the LiTA12 detector system (described in Sec. IV A 3) set at L_S = 19 m, and the results are shown in Fig. 9(b). The borosilicate glass and cadmium plates were found to be almost transparent above 1 eV and 0.45 eV, respectively, while the acrylic resin reduced neutron intensity to about half in the range from 1 eV to 1 keV and then dropped off quickly at lower neutron energies. The Pb and Bi filters, on the other hand, attenuated higher energy neutrons above about 1 eV while maintaining neutron intensity at lower energies. Figure 9(c) shows the relative neutron intensity at 1 eV as a function of Pb or Bi thickness, which decreases exponentially as expected. The neutron intensity with the 5-mm-thick acrylic resin plate is also shown for comparison.

IV. NEUTRON IMAGING DETECTORS AT RADEN

At RADEN, we have prepared various neutron imaging detector systems to meet the very different needs of both energy-resolved neutron imaging and traditional radiography and computed tomography. These include advanced, counting-type imaging detector systems for energy-resolved techniques and conventional camera systems for radiography and tomography.

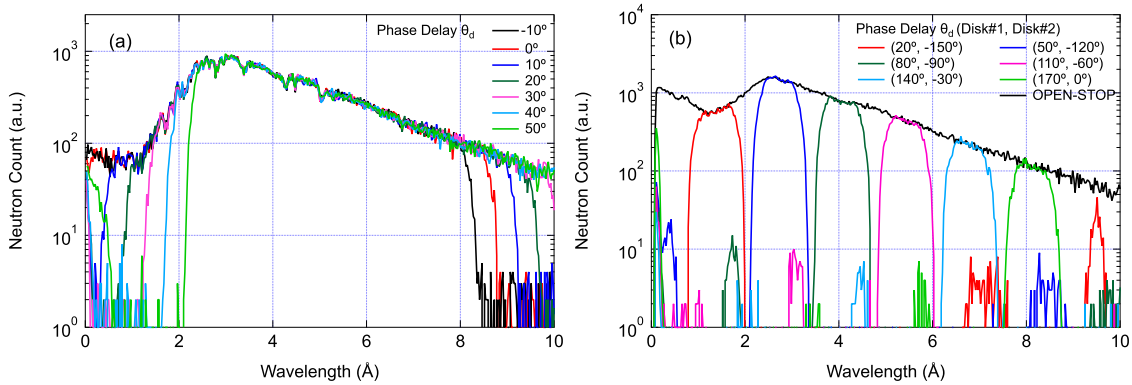

FIG. 8. Neutron beam spectra measured for various double-disk chopper conditions. The T0 chopper was stopped for all measurements. (a) Phase delays of Disk#1 and Disk#2 were the same (100 mm-thick Bi filter was in the beam). (b) Narrowest bandwidth case with the opening angle set to 20° between Disk#1 and Disk#2.

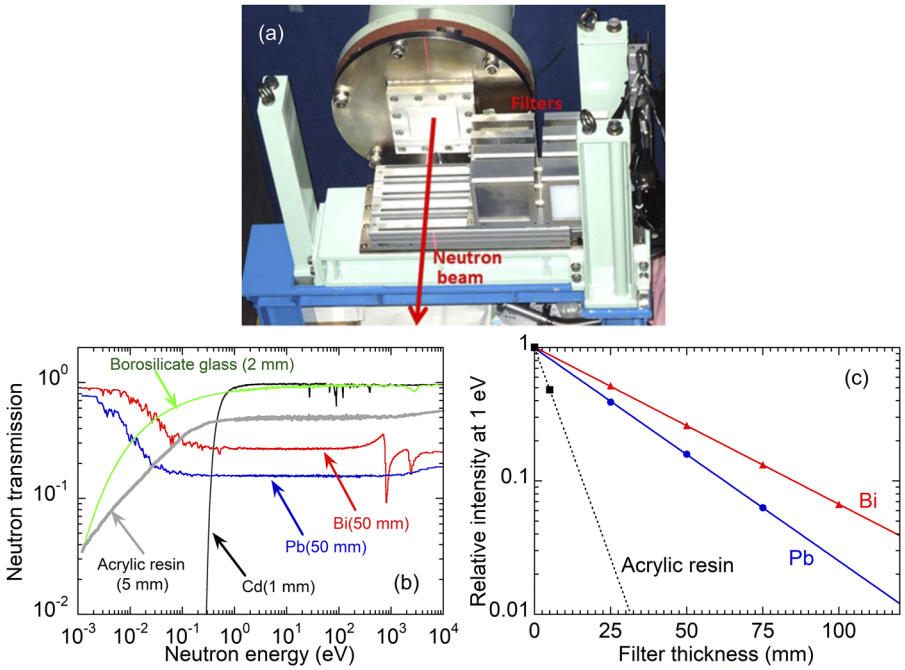

FIG. 9. (a) Photograph of the beam filter insertion device, (b) neutron energy-dependent transmission rates of the filters measured by the LiTA12 detector system, and (c) neutron transmission rates at 1 eV as a function of filter thickness for Pb, Bi, and acrylic resin filters. Lines are the results of fitting by an exponential function.

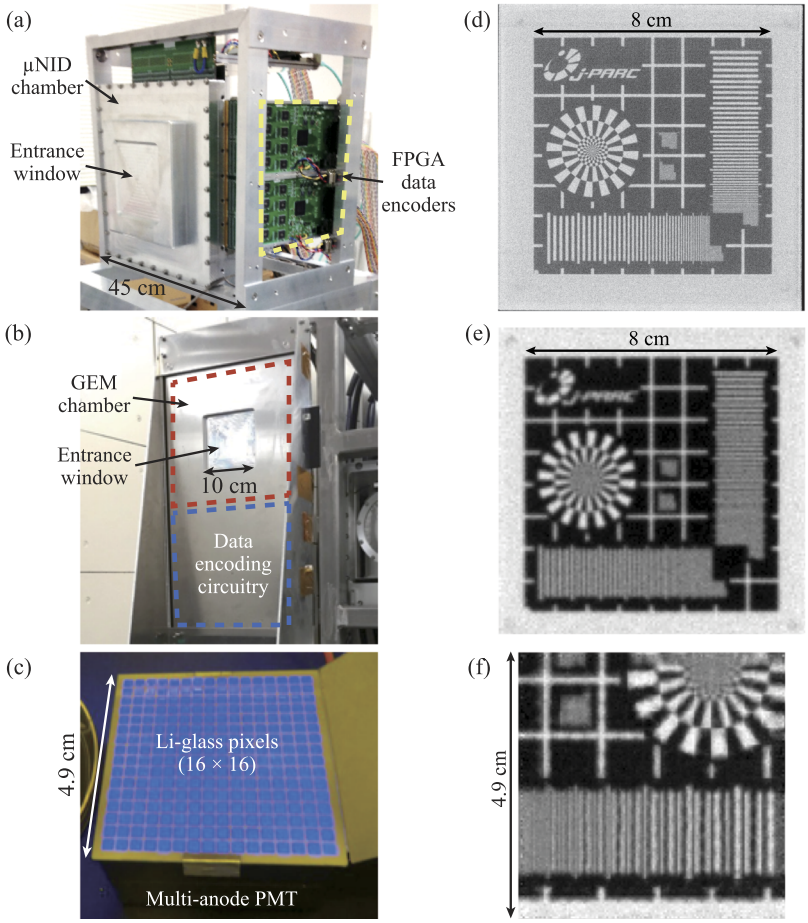

FIG. 10. Counting-type detectors at RADEN. Shown here are photographs of the micropattern detectors μNID (a) and nGEM (b), and the Li-glass scintillator pixel detector LiTA12 (c) currently in use at RADEN for energy-resolved neutron imaging. Example images of a Gd test target taken at RADEN are shown in (d)–(f) for the corresponding detector on the left.

A. Counting-type detectors

For carrying out energy-resolved neutron imaging in the high-rate, high-background environment at RADEN, we use cutting-edge detector systems, which were developed in Japan, employing micropattern detectors or fast Li-glass scintillators, coupled with high-speed FPGA (Field Programmable Gate Array)-based data acquisition (DAQ) systems. These counting-type detectors measure each incident neutron event to achieve the sub-μs time resolution necessary for the accurate determination of neutron energy via time-of-flight and provide for event-by-event background rejection.

The photographs of the counting-type imaging detector systems currently available at RADEN are shown in Figs. 10(a)–10(c) along with images of a Gd test target[32] taken at RADEN in Figs. 10(d)–10(f) for each detector. The detector systems include the μNID,[33] a micropattern detector developed at Kyoto University and manufactured by Dai Nippon Printing Co., Ltd., and the nGEM micropattern[34] and LiTA12 Li-glass scintillator pixel detectors,[35] both developed at KEK and manufactured by Bee Beans Technologies Co., Ltd., and Japan Neutron Optics, Inc., respectively. These detectors cover a range of spatial resolutions from several millimeters down to 100 μm and provide neutron counting rates up to 8 Mcps. Additionally, the μNID and nGEM detectors can be controlled via the MLF standard instrument control software framework (IROHA2), described in Sec. V A, allowing for automated measurements. The main performance features of these detectors are listed in Table IV, and each is discussed below in more detail.

1. μNID—μPIC-based neutron imaging detector

The μNID, shown in Fig. 10(a), is based on a time projection chamber (TPC) with an active gas volume of 100 × 100 × 25 mm^3 and a micro-pixel chamber (μPIC) micropattern readout plane. The μPIC has a 0.4-mm-pitch, two-dimensional strip readout that is coupled to an FPGA-based modular data acquisition system for fast data processing. To facilitate neutron detection, the detector vessel is filled with a gas mixture of CF_4–iC_4H_{10}–^{3}He (45:5:50) at a total pressure of 2 atm, providing a detection efficiency of 26% for thermal neutrons. The charged particles released by the absorption of a neutron on a ^{3}He nucleus, namely, a proton and a triton, deposit energy inside the active volume of the TPC by ionizing atoms within the gas, stopping in a combined distance of about 4 mm. The cloud of liberated electrons then drifts along an applied electric field of 1600 V/cm at constant velocity to the μPIC, where the electrons undergo gas amplification and produce analog signals on the readout strips. The three-dimensional track (two-dimensional strip readout plus arrival time) and energy deposition (measured as the time for which the analog signal on a strip exceeds a preset threshold voltage, referred to as *time-over-threshold*) of the resultant proton–triton pair are recorded in the FPGA-based data encoder modules[36] and sent to a personal computer (PC) via Gigabit Ethernet. This detailed tracking information allows the μNID to achieve the fine spatial resolution of 0.1 mm (at a modulation transfer function value, or MTF, of 10%) shown in Fig. 10(d) and an excellent γ-ray sensitivity of less than 10^{-12}. The μNID also features a time resolution of 250 ns, a peak count-rate capacity of 8 Mcps, and an effective peak count-rate of 1 Mcps at less than 2% event loss.[37] The development of the μNID system is being actively pursued at RADEN, with efforts to improve the spatial resolution and rate performance underway, as described in Ref. 37.

TABLE IV. Performance of counting-type detectors at RADEN. The values for the spatial resolution, peak count-rate capacity, and effective peak count-rate were confirmed at RADEN, where "peak count-rate capacity" and "effective peak count-rate" refer to the global instantaneous peak rates (i.e., peak rates over the entire detection area) at the absolute limit of the DAQ hardware and with less than 2% event loss, respectively.

Detector	μNID	nGEM	LiTA12
Type	Micropattern	Micropattern	Scintillator
Neutron converter	^{3}He	^{10}B	^{6}Li
Area (mm^2)	100 × 100	100 × 100	49 × 49
Time resolution (ns)	250	15	40
Spatial resolution (mm)	0.1	1	3/0.7
Efficiency @25.3 meV (%)	26	10	23
Peak count-rate capacity	8 Mcps	4.6 Mcps	8 Mcps
Effective peak count-rate	1 Mcps	180 kcps	6 Mcps

2. nGEM—Boron-coated gas electron multiplier

The nGEM detector, shown in Fig. 10(b), uses a time projection chamber incorporating a drift cathode and a GEM (gas electron multiplier), each coated with a thin layer of ^{10}B (~1 μm) to facilitate neutron detection, thereby achieving a detection efficiency of about 10% for thermal neutrons. The reaction of a neutron with ^{10}B produces charged particles in the form of an alpha particle and a ^{7}Li nucleus, one of which may escape the boron layer and enter the Ar–CO_2 (70:30, 1 atm) filling gas of the detector. The charge liberated in the gas by this charged particle is amplified by a pair of normal GEMs and then read out via a 0.8-mm-pitch, two-dimensional strip plane. These signals are processed by an FPGA-based data acquisition board, and the resulting digitized neutron event data are recorded to a PC via Gigabit Ethernet. By measuring the mean position of the charge distribution of the resultant alpha or ^{7}Li track, the nGEM detector achieves a spatial resolution of about 1 mm, as illustrated in Fig. 10(e). The nGEM also features an excellent time resolution of 15 ns, a γ-ray sensitivity of 10^{-4}, and a peak count-rate capacity of 4.6 Mcps, with an effective peak count rate of 180 kcps at 2% event loss. The spatial resolution and rate performance of the nGEM were confirmed through on-beam tests at RADEN, as previously reported in Ref. 37. The γ-ray sensitivity of the nGEM is worse than that of the μNID of Sec. IV A 1 due to the differences in the neutron conversion mechanism and subsequent data analysis, but it is still sufficient for energy-resolved neutron imaging experiments at RADEN.

3. LiTA12—^{6}Li time analyzer, model 2012

The LiTA12 (^{6}Li Time Analyzer, Model 2012) Li-glass scintillator pixel detector, shown in Fig. 10(c), consists of a 16 × 16 array of ^{6}Li-impregnated, cerium-activated glass scintillator pixels (scintillator type GS20), each of size 2.1 × 2.1 × 1 mm^3. The scintillator pixels are fixed in an opaque support frame, which both optically isolates each pixel and matches the pixel spacing to a Hamamatsu H9500

multi-anode photomultiplier (MA-PMT) with an anode pitch of 3 mm and covering a total area of 49 × 49 mm^2. Charged particles from the neutron–^{6}Li interaction (i.e., an alpha and a triton) produce scintillation light that is then converted to an electronic signal by the MA-PMT. The signals from each anode pass through a front-end amplifier module and are then digitized in custom FPGA modules. The LiTA12 pixel detector achieves a detection efficiency of about 23%, a peak count-rate capacity of 8 Mcps, and a high effective peak count-rate of 6 Mcps at less than 2% event loss, but, since each pixel is optically isolated, its spatial resolution is limited to the pixel pitch of 3 mm.[38]

In an alternate configuration, the Li-glass pixels are replaced by a single scintillator plate that covers the entire area of the MA-PMT. In this case, the light from a single neutron event spreads over multiple anodes, allowing a more precise determination of the position from the centroid of the resulting charge distribution. In testing of the LiTA12 with scintillator plate at the MLF, a spatial resolution of about 0.7 mm was confirmed using the charge-centroid technique [see Fig. 10(f)].[39] The LiTA12 with scintillator plate is now being investigated for use as a detector for neutron resonance absorption imaging measurements, since the efficiency for epithermal neutrons can easily be increased by increasing the thickness of the scintillator plate.

B. Camera-type detectors

The schematic illustration of a camera-type detector used at RADEN for radiography measurements is shown in Fig. 11. Neutrons that penetrate the sample are converted to visible light by a ^{6}LiF + ZnS scintillator screen with thickness from 50 μm to 200 μm made by RC TRITEC AG and then are focused on the camera sensor by an aluminum-coated quartz mirror and optical lenses. The surface of the mirror is coated with a dielectric multilayer, and its reflectivity is designed to be more than 98% in the wavelength range from 430 nm to 550 nm. Typical optical lenses employed by the system are Nikon prime lenses (50 mm f/1.4, 85 mm f/1.4, and 105 mm f/1.4) and a SIGMA macrolens (150 mm f/2.8). At RADEN, it is possible to select a suitable camera-type detector from the available camera lineup (including a back-illuminated CCD camera, ANDOR iKON-L 936, 2048 × 2048 pixels; an electron multiplying CCD camera, ANDOR iXon Ultra 888, 1024 × 1024 pixels; and a scientific CMOS camera, PCO pco.edge gold 4.2, 2048 × 2048 pixels) according to the experimental purpose, such as high-resolution radiography or high-speed radiography and tomography. All cameras are water-cooled to suppress dark current noise and are mounted on a motorized vertical linear motion stage. By changing the distance between the camera sensor and scintillator screen using this stage, the FoV can be adjusted continuously in the range from 20 × 20 mm^2 to 300 × 300 mm^2. These detector components are placed in a black aluminum box shielded with thick lead plates and ^{10}B$_4$C-impregnated rubber sheets to reduce undesirable noise due to scattered neutrons, γ-ray irradiation, and leaked light. The camera system can be controlled through the IROHA2 instrument control software framework (Sec. V A), and in the case of neutron tomography measurements, both the camera-type detector and a rotary stage are sequentially controlled with IROHA2.

Figure 12 shows a transmission image of the Gd test target taken with a FoV of 20 × 20 mm^2 and a L/D of 398 using the back-illuminated CCD camera and a ^{6}LiF + ZnS scintillator screen of 50 μm thickness. The exposure time was 150 s at the proton beam power of 300 kW. The test target was placed directly on the surface of the scintillator screen. A spatial resolution of 30 μm, determined as the smallest line-pair spacing that can be visually discerned within the transmission image, was achieved with this camera setup [Fig. 12(b)]. In general, the spatial resolution for a given camera setup depends on several factors, with the scintillator thickness/composition and FoV (or more precisely, the pixel size within a given FoV) being the main determining factors. The spatial resolutions when using a 50 μm-thick ^{6}LiF + ZnS scintillator screen were found to be about 40 μm (FoV = 50 × 50 mm^2) and 70 μm (FoV = 100 × 100 mm^2), and the spatial resolutions when using a 100 μm-thick ^{6}LiF + ZnS scintillator screen were about 140 μm (FoV = 150 × 150 mm^2), 200 μm (FoV = 200 × 200 mm^2), and 300 μm (FoV = 300 × 300 mm^2).

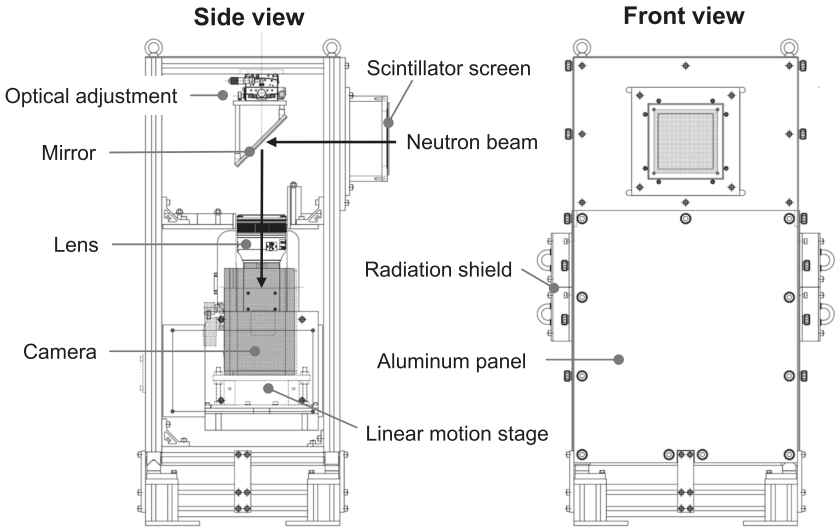

FIG. 11. Schematic illustration of the camera-type detector. Neutrons are converted into visible light by the scintillator screen, and the light is reflected toward the camera sensor by a mirror. The distance between the camera sensor and scintillator screen can be adjusted by using a motorized vertical stage.

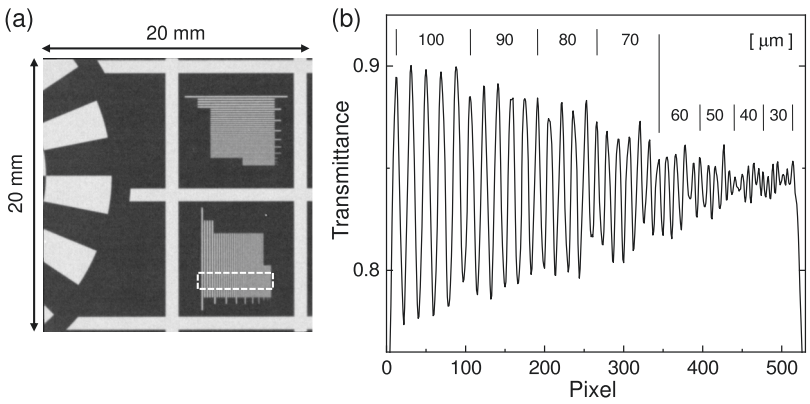

FIG. 12. (a) Transmission image of a Gd test pattern and (b) the averaged line profile of the rectangular region surrounded by the dashed line in (a).

Additionally, the spatial resolution for neutron tomography was studied using a test sample with three-dimensional structure. Figures 13(a) and 13(b) show a photograph and a transmission image (radiograph), respectively, of the test sample taken with a FoV of 56 × 56 mm^2 and a L/D of 398 using the back-illuminated CCD camera and the ^{6}LiF + ZnS scintillator screen of 50 μm thickness. The exposure time for the radiograph was about 80 s at the proton beam power of 300 kW. The test sample consists of stacked pairs of thin stainless-steel and aluminum plates, which are held in an aluminum housing and pressed from one side with screws. The widths and spacings of the stainless-steel plates were adjusted by changing the stacking number of both types of plates, and the actual values are indicated in Fig. 13(a). The distance from the rotation axis of the test sample to the scintillator screen was 55 mm, giving a geometric blurring of 0.14 mm on the scintillator screen; thus, line pairs smaller than 200 μm thickness could not be identified in the radiograph of Fig. 13(b).

For the tomography measurement, projection images were obtained by the half-scan method, i.e., rotating the sample from 0° to 180° by 1° steps, and the tomograms were reconstructed using the filtered-back-projection (FBP) algorithm. Figure 13(c) shows the resulting tomograms in the xy and xz planes of the test sample. The observed widths and spacings for the stainless-steel plates were 0.96 mm, 0.72 mm, 0.58 mm, 0.48 mm, 0.40 mm, 0.29 mm, and 0.21 mm, which were reasonably close to the actual values. As in the case of the radiograph, the line pairs of 0.10 mm thickness were difficult to identify from the tomograms due to geometrical blurring. Consequently, the achievable spatial resolution of a tomogram was determined to be 0.20 mm or less from this experiment.

V. SOFTWARE

A. Instrument control

Because the RADEN instrument is composed of many devices, including a variety of optical devices, several detectors, and various optional equipment, an integrated and easy-to-use operation/control system is indispensable to allow even less-experienced users to conduct experiments smoothly and efficiently. The IROHA2 software framework, which is the standard instrument control software framework of the MLF, has been adopted at RADEN.[40] Additionally, the DAQ-Middleware framework, developed at KEK[41] and used as the standard data acquisition software at the MLF for efficient event recording,[42] has been introduced as the data acquisition software for the counting-type detectors of RADEN.

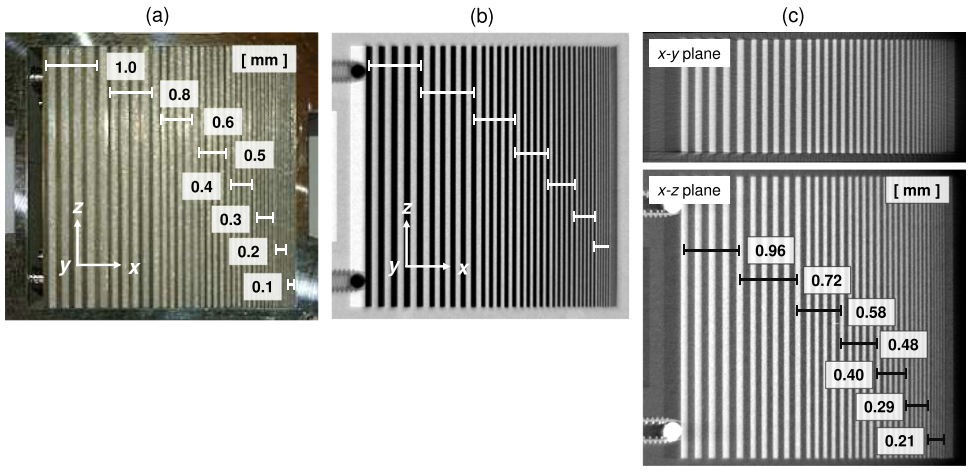

FIG. 13. (a) Photograph, (b) radiograph, and (c) xy and xz plane tomograms of the test sample. The actual widths and intervals of each stainless-steel pairs are given in the inset of (a), and the calculated values from the line profile of the tomograms are given in the inset of (c).

The IROHA2 framework consists of four software components: (1) the device control server to control devices and monitor their status, (2) the instrument management server to authenticate users, manage a measurement, and configure instrument setup, (3) the sequence management server to setup and perform automated measurements, and (4) the integrate control server to unify instrument control and monitoring, and summarize the current instrument status of the measurement, devices, and facility. In particular, IROHA2 is very efficient for performing measurements of time-transient phenomena because the status of each device and/or the condition of the sample environment, such as magnetic field strength, temperature, and electric current/voltage, is logged and recorded as time-series data together with the neutron event data. At RADEN, three device servers are used for controlling and logging the status of devices: one for optical devices such as choppers, filters, and collimators; one for devices for polarization analysis such as power-supplies, function generators, and digital multimeters; and one for the remaining devices including sample stages, other motorized equipment, and camera systems. With IROHA2, we can use all the functions of the software components via a web interface, shown in Fig. 14, for example, which provides users good visibility of the experimental status and the capability of easy operation. Moreover, because the server outputs a static HTML file to the web server, which is accessible from the Internet, we can view the current status of the instrument from anywhere.

For computed tomography measurements, which require repeating sequential control of both image acquisition and stage rotation over many iterations, a unique measurement system is prepared at RADEN and included in the sequence management server. Because J-PARC is a multi-purpose accelerator facility, some of the proton pulses are distributed to other experimental facilities within J-PARC every few seconds, and the accidental accelerator trip may also happen occasionally. To prevent neutron intensity deviation and possible dropping of images during a computed tomography measurement, image acquisition with the camera system is controlled via the proton pulse shot-count. In addition, to shorten the dead time at each image acquisition as much as possible, we have added a command to the sequence management server that unifies the stage rotation, shot counting, and image acquisition into a single command. Using this command, it becomes possible to automatically perform computed tomography measurements with changing experimental conditions with the IROHA2 system.

Additionally, within the IROHA2 system, there is a supplementary function to include equipment brought to RADEN by users, such as a prototype detector or a custom-made load frame, under the control of IROHA2. With the help of this function, we can perform automatic measurements using such equipment along with the standard devices equipped in RADEN.

B. GUI-RITS

Data analysis software for the Bragg-edge transmission (BET) spectrum, the Rietveld Imaging of Transmission Spectra (RITS) code, was originally developed by Sato[4] written in the Fortran programming language without a Graphical User Interface (GUI). Now, the program has been coded as a GUI program written in C++, referred to as GUI-RITS, providing improved ease-of-use and increased execution speed. The program can read single or multiple spectra and can perform total-pattern or single-edge analyses.

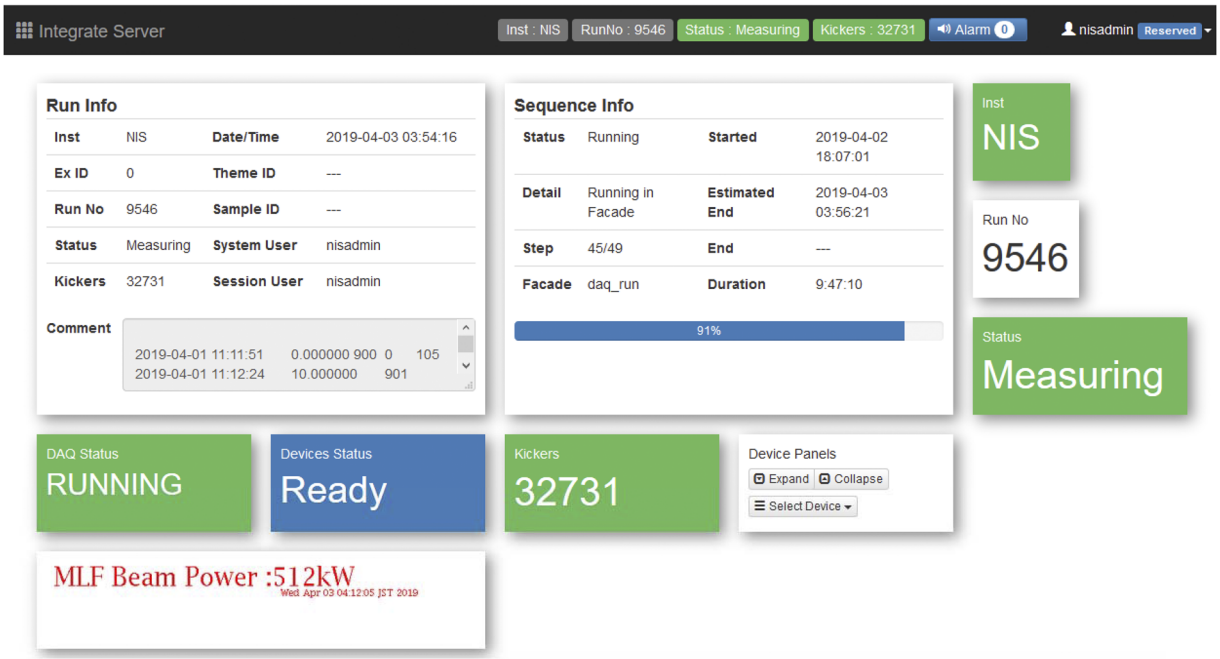

FIG. 14. Screenshot of the integrate control server interface at RADEN. This web page can be viewed via the Internet for offsite monitoring of an experiment.

GUI-RITS can also execute multithreaded calculations for improved performance. GUI-RITS currently supports only the Linux platform.

An example of a GUI-RITS analysis of a duplex stainless steel is shown in Fig. 15. The initial parameters for each phase, phase 1 for ferrite and phase 2 for austenite, are input on the corresponding tabs of the initial parameter input panel, as shown in Fig. 15(a), where a check mark on the right side of the input cell turns each parameter on or off in the refinement. The refined BET spectrum is displayed in Fig. 15(b) as a function of neutron wavelength. The RITS execution panel in Fig. 15(c) shows the progress of the refinement and the convergence values and their standard deviations.

VI. DEMONSTRATION

A. Bragg-edge imaging

A BET spectrum contains the microscopic information of a crystalline material, such as the crystallographic texture and

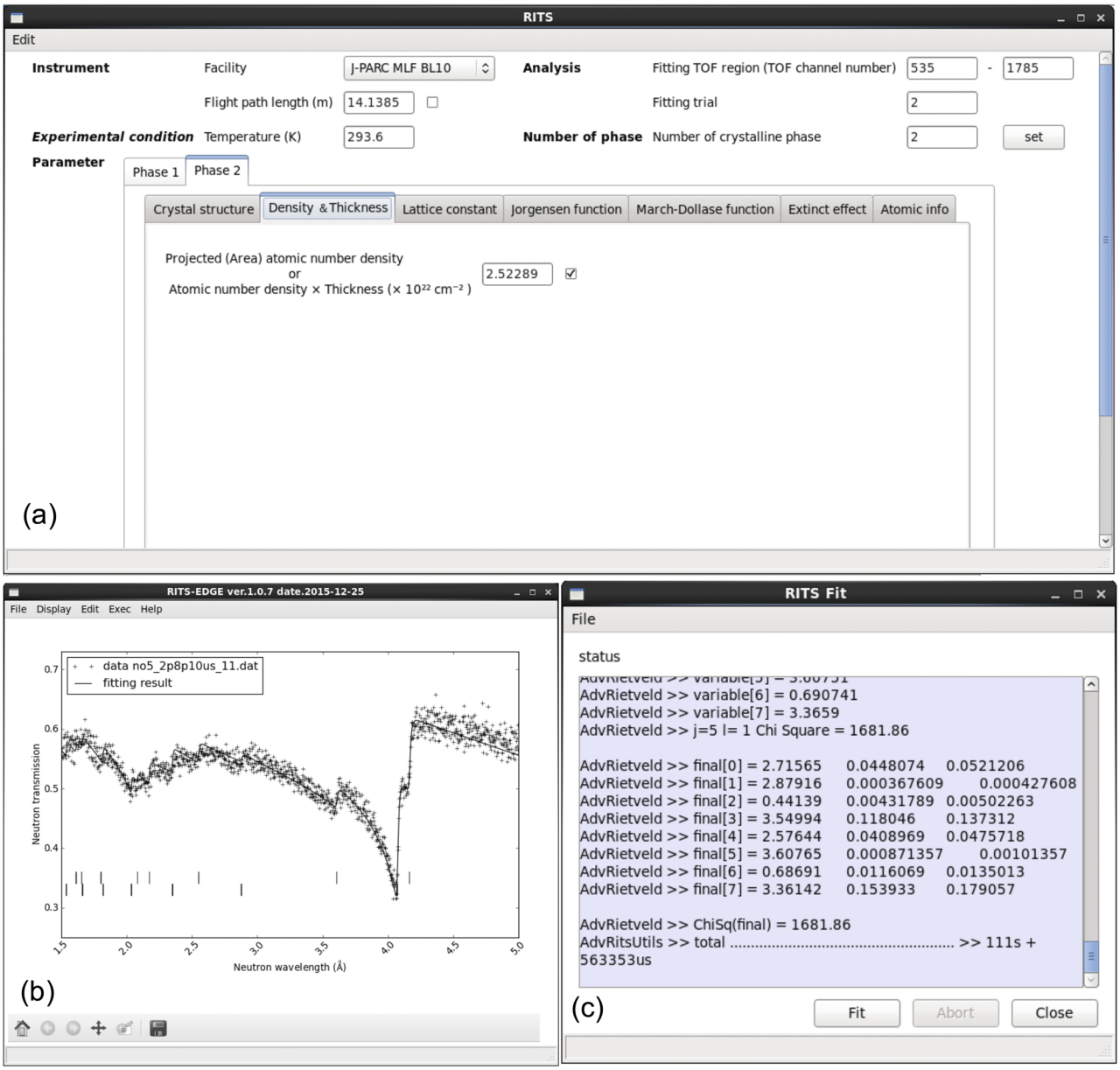

FIG. 15. Screenshots of GUI-RITS. (a) RITS initial parameter input panel. (b) Data viewer for the analyzed transmission data. (c) RITS execution panel.

microstructure, which can be quantitatively analyzed by the GUI-RITS code. By the analysis of the position-dependent BET spectra, we can obtain two-dimensional maps of the quantitative structure information, known as Bragg-edge imaging, where the resolution of a Bragg edge is analogous to that of the Bragg peak analyzed in neutron diffraction.

The BET spectrum of a piece of ferrite steel with dimensions of 20 × 10 × 2 mm^3, which has been used for the reference peak-shape of the engineering diffractometer TAKUMI in the MLF,[43] was measured at RADEN using the nGEM detector placed at a position of L_S = 23.8 m. An example of the Bragg edge for the ferrite 110 is shown in Fig. 16(a) along with its derivative data. The estimated FWHM (63 μs; FWHM = $\sqrt{8 \ln 2}\sigma$) is marked by a two-way arrow, and the Bragg-edge position (24 433 μs) is indicated by the dashed vertical line. Additionally, the slightly asymmetric ±3σ position is shown by dashed–dotted vertical lines. The derivative data were fit by the convolution of back-to-back exponentials and a Gaussian function.[44] Convolution of this fit function with the Heaviside step function[45] produces the edge-profile shape function of the GUI-RITS code. The effective Bragg-edge resolution was around 0.26%, which was somewhat worse than the intrinsic wavelength resolution (i.e., 0.2% at the 23 m position of RADEN[19]). Figure 16(b) shows the observed and calculated BET spectrum, with vertical marks indicating the positions of Bragg edges. The difference of the observed and calculated spectra is also shown (offset by +0.55). Every Bragg edge shows a particularly sharp drop in the transmission; however, there are complicated billows visible between the edges. The texture analysis using GUI-RITS revealed that the billows originate from strong 110 and 111 textures oriented perpendicular and parallel to the incident beam, respectively, in a contribution fraction of 0.73:0.27.

Additionally, Bragg-edge imaging can help us to understand the phase transformation mechanisms of materials. We applied this method to directly visualize inhomogeneous phase transformation in a steel material, the martensite transformation in a metastable austenitic alloy Fe–25Ni–0.4C (by wt. %) with applied stress followed by sub-zero treatment. Bragg-edge imaging experiments were performed using the nGEM detector placed at L_S = 23.8 m. The

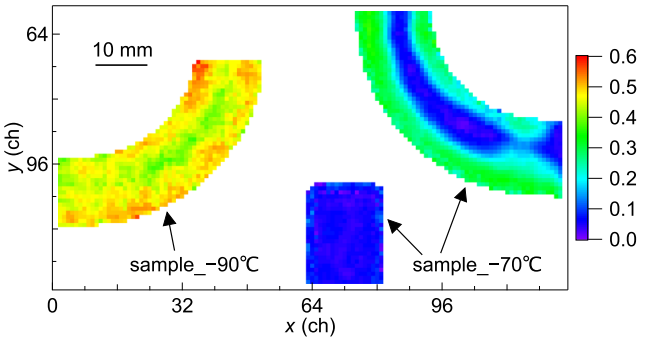

FIG. 17. Two-dimensional map of the volume fraction of the martensite phase in a metastable austenitic alloy after sub-zero treatment at −70 °C and −90 °C.

L/D value was 1000. The details of the sample preparation, experimental procedure, and data analysis were described in the Refs. 46 and 47. Figure 17 shows the quantitative two-dimensional map of the volume fraction of the martensite phase obtained by the RITS analysis. First, the unstressed reference sample, visible as the rectangle in the lower-middle of Fig. 17, shows little martensite phase formation arising from the −70 °C treatment alone. In the bending sample shown in the upper-right of Fig. 17, the martensite phase was detected preferentially in the outer (tension) and inner (compression) regions after treatment at −70 °C, where the residual strains were strongly formed by the bending. For the bending sample in the left of Fig. 17, the martensite phase volume fraction markedly increased after the −90 °C treatment; however, the effect of weak deformation was still visible around the central region of the sample.

B. Resonance absorption imaging

Neutron-induced reaction cross sections rapidly increase at particular resonance energies specific to a target nuclide, and neutron resonance absorption imaging utilizes these resonance reactions to visualize distributions of specific nuclides in a sample.

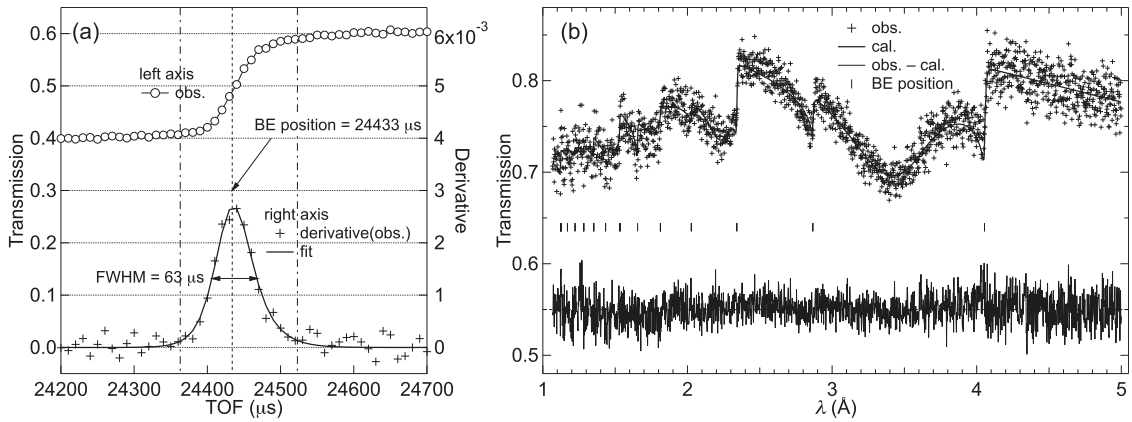

FIG. 16. (a) 110 Bragg edge of a ferrite steel and its derivative data with a fitting curve. (b) Full BET spectrum of the ferrite steel and the RITS analysis pattern.

In resonance absorption imaging, neutrons are transmitted through a sample and are then detected by a time-analyzing two-dimensional detector. The spatial distribution of the density or temperature for a specific nuclide can be derived by analyzing the corresponding dip(s) in the energy-dependent transmission curve point-by-point over a sample. Since the neutrons are transmitted through the sample, the obtained distribution carries integrated information along the entire penetration path. This feature allows resonance absorption imaging to be extended to three-dimensions (via computed tomography techniques), providing an advantage over fluorescent x-ray spectroscopy, which can only analyze elements at the surface of a sample. This technique is expected to be provided for general use at RADEN, taking advantage of the high energy resolution of the short-pulsed neutron source at the MLF.

A demonstration measurement using 1- and 2-euro coins and 0.5-mm-thick Cu and 0.4-mm-thick Zn plates is shown in Fig. 18. The measurement was performed with the nGEM detector at RADEN. The proton beam power was 300 kW, and the L/D was 667. The neutron transmission rates as a function of energy for the Cu and Zn plates are shown in Fig. 18(b), where many resonance dips are clearly visible. The largest dips were recognized at 517 eV and 2.04 keV in the spectra of Zn and Cu, respectively. The neutron transmission rate of the 0.5-mm-thick copper plate was 0.30 at the resonance energy of 2.04 keV. Assuming that the minimum thickness accessible to the resonance absorption technique is that giving a neutron transmission rate of 0.90 at a given resonance energy, the minimum thickness of copper was calculated as 0.044 mm from the above observed transmission rate. In the same manner, that of zinc

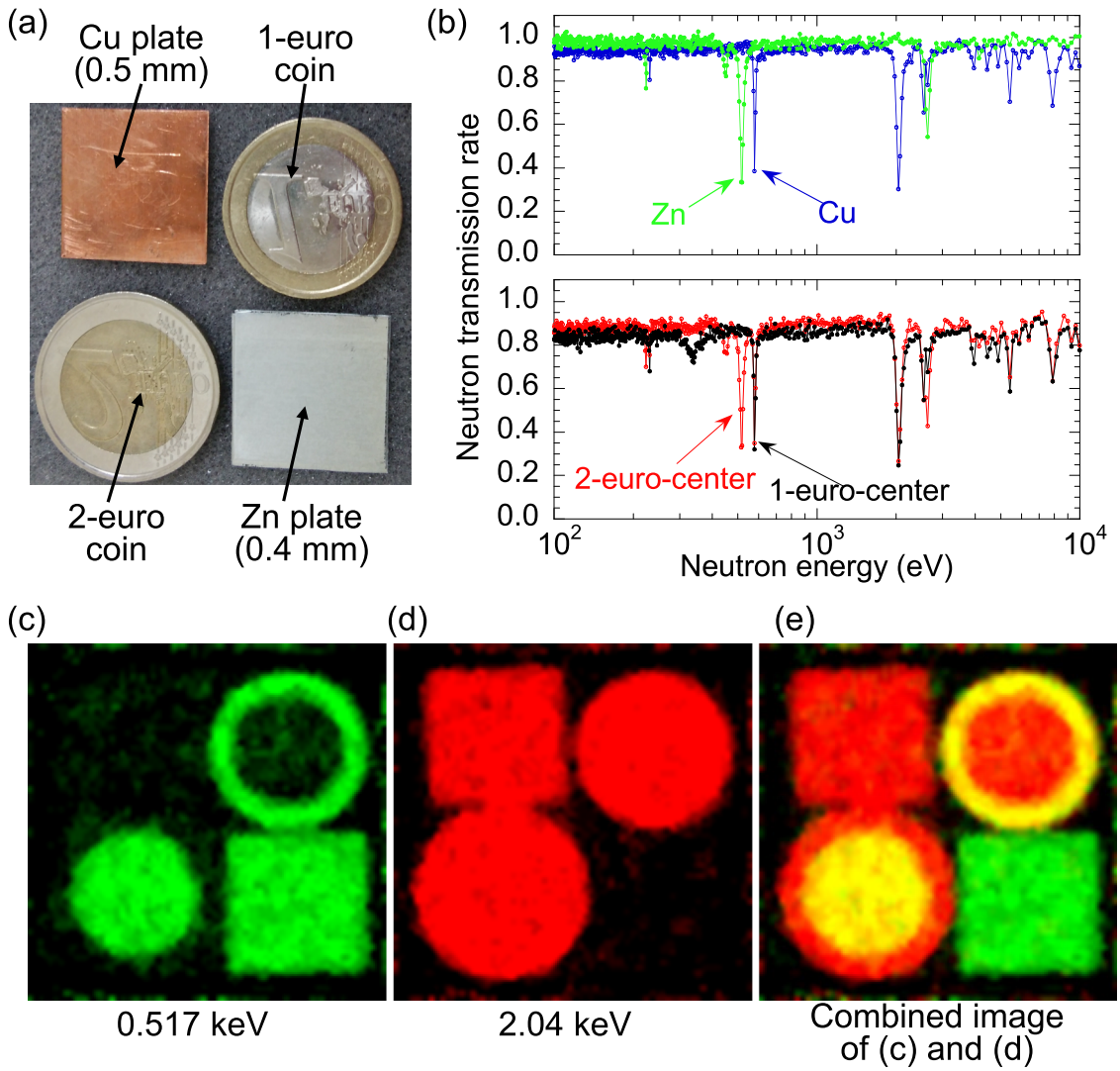

FIG. 18. (a) Photograph of samples, including 1- and 2-euro coins and Zn and Cu plates. (b) neutron transmission rates of the samples. Radiographs are also shown for neutron energies of (c) 0.517 keV, (d) 2.04 keV, and (e) combined image of (c) and (d).

was derived to be 0.038 mm from the transmission rate (0.33) of the 0.4-mm-thick zinc plate at 517 eV. The minimum thicknesses can be reduced by adopting a higher transmission rate for the definition; however, it requires better statistical uncertainties and is rather unrealistic at present considering the maximum counting rates of available detectors, spatial resolution, and time of measurement. The spectrum of the central part of the 1-euro coin exhibited dips at the same energies as the Cu plate, while the dips in the spectrum of the central part of the 2-euro coin were seen at the energies of both Cu and Zn. This indicated that the former part contains Cu and the latter contains both Cu and Zn. Neutron transmission images for neutron energies of 517 eV and 2.04 keV are shown in Figs. 18(c) and 18(d), indicating the spatial distributions of Zn and Cu, respectively. It should be noted that the 0.4-mm-thick Zn plate was clearly visualized using the resonance absorption technique, even though the transmission rate was 99% for cold neutrons at RADEN. This demonstrates the advantage of the enhanced sensitivity using this energy-resolved method. Figure 18(e) shows a combined image of Figs. 18(c) and 18(d). The distributions of Zn and Cu were indicated by green and red, respectively. Thus, the areas containing both Zn and Cu were shown as yellow, i.e., as a mixture of green and red.

C. Polarized neutron imaging

There are many magnetic imaging techniques to study magnetic materials, such as Kerr microscopy, magnetic force microscopy (MFM), photoemission electron microscopy (PEEM) using X-ray magnetic circular dichroism (XMCD), and so on. As a neutron possesses a magnetic moment arising from its spin, a neutron can directly interact with a magnetic field. The combination of imaging and neutron spin information provides a very unique opportunity to visualize magnetic field distributions in both free space and within materials.[48] Especially, the neutron's penetration capability, which allows it to sense the magnetic field within a bulk material, not only at the surface, provides a big advantage compared with other techniques. With this high penetration capability, the specially prepared sample with a polished mirror surface or reduced thickness, for example, is not necessary for the neutron experiment, enabling the study of the original properties of the object. Moreover, owing to the direct interaction between the neutron magnetic moment and the magnetic field, the quantification of the magnetic field is simpler than other techniques using the magneto-optical effect for which the electronic states of the object must be known. Several techniques using the neutron beam have been developed,

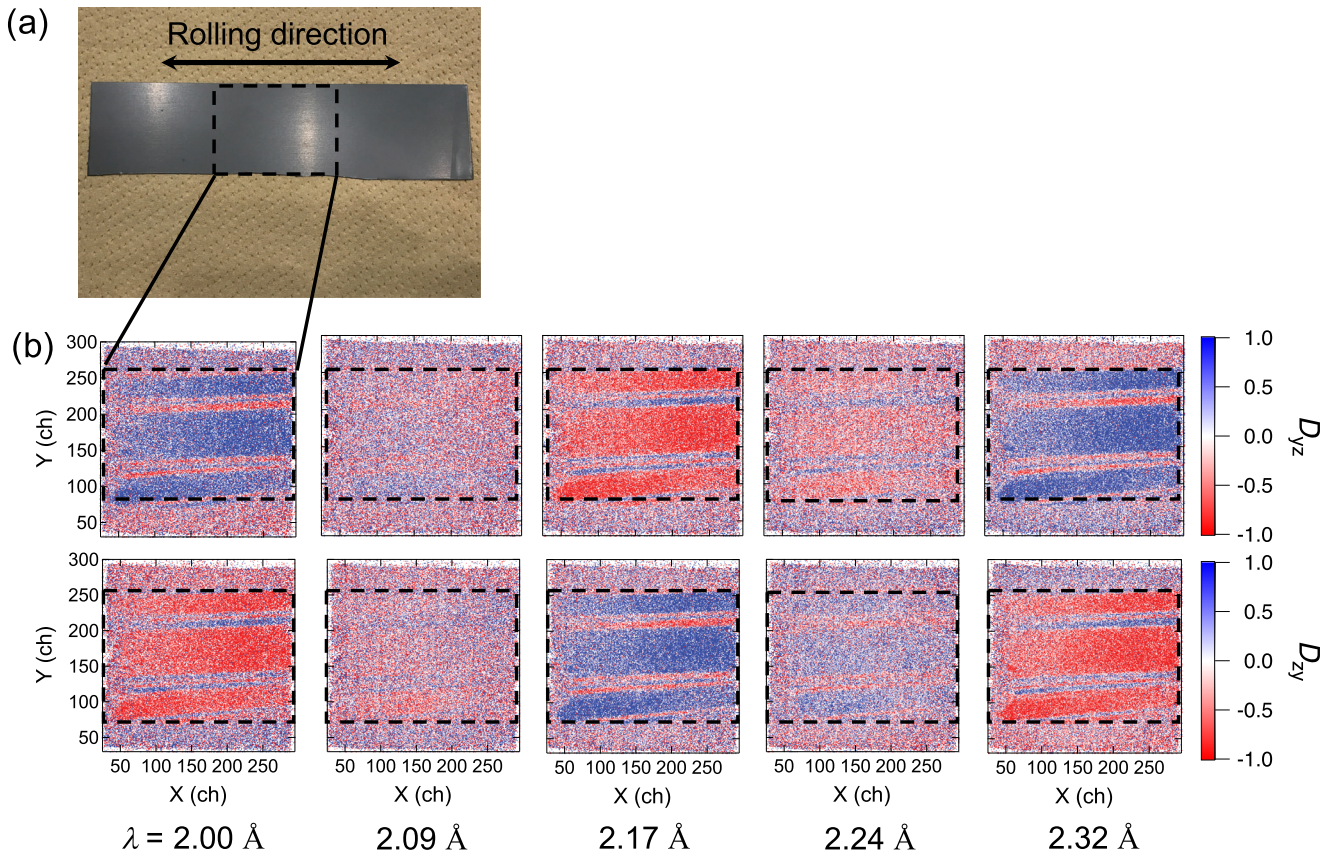

FIG. 19. (a) A Photograph of the GO steel sample. (b) Wavelength dependence of the polarization distribution images for D_{yz} and D_{zy} (1 ch = 0.2 mm). The wavelength resolution of these images is 0.021 Å. Dashed rectangles indicate the position of the GO steel sample within each polarization image.

i.e., polarization analysis,[13] neutron spin phase contrast,[49] and neutron phase imaging using the Talbot-Lau interferometer.[50] The fundamental idea of magnetic field imaging using the polarized neutron beam is described in Refs. 13, 48, and 51, but here we briefly introduce the benefits of pulsed neutrons. In the view of the classical mechanism, a neutron magnetic moment precesses around a given magnetic field with an angular velocity proportional to the field strength, which is the well-known Larmor precession. The resulting precession angle, which is proportional to both the path integral of the field strength and the neutron wavelength, can be analyzed as a change in the neutron polarization. When using a monochromatic neutron beam, it is intrinsically impossible to distinguish the precession angle greater than π since an arbitrary number of rotations may occur unobserved between the initial and final polarization states. This problem can be overcome by analyzing the wavelength dependence of neutron polarization, and consequently, the quantification and visualization of the magnetic field strength distribution becomes possible.[13] Moreover, employing three-dimensional polarization analysis (polarimetry) in combination with the wavelength-resolved measurement also makes it possible to extract directional information of the magnetic field together with its strength. At RADEN, a ToF polarimetry apparatus is installed in front of the near sample position.[52] All devices can be positioned in the beam using motorized exchangers, enabling easy switching between the polarized and unpolarized beam setup.

As an example of application studies using pulsed polarized neutron imaging, we have performed the visualization of the magnetic domain structure in a grain-oriented (GO) magnetic steel.[53] The sample consisted of a surface coated Fe–Si 3 wt. % GO steel with a thickness of 0.23 mm [Fig. 19(a)]. This sample was placed so that its rolling direction was parallel to the x direction. The μNID detector was used as a two-dimensional neutron detector, and the L/D was set to 1300 using beam slits installed in the upstream optics section.[20] The resulting image blurring due to this beam collimation was expected to be about 0.58 mm, according to the distance between the sample and detector of 0.75 m. The polarization distribution images for the D_{yz} and D_{zy} polarization matrix elements, where D_{ij} refers to the normalized polarization with the incident spin direction along i and the outgoing analyzed spin direction along j, where $i, j = x, y, z$, were taken in order to analyze the x-component of the magnetization inside the GO steel. These matrix elements were measured since the main component of the magnetization was expected to lie along the rolling direction (i.e., x direction) and the terms D_{ij} and D_{ji} with $i \neq j$ contain an oscillatory component that is sensitive to the field direction orthogonal to the i and j axes.[54] Figure 19(b) shows polarization distribution images for D_{yz} and D_{zy} for several wavelengths. The polarization degree within the area of the steel sample, indicated by the dashed lines in Fig. 19(b), appear to change periodically against neutron wavelength, and the signs of D_{yz} and D_{zy} at the same wavelength were opposite to each other. These behaviors give clear evidence that the steel magnetization indeed lies parallel to the rolling direction. The integrated magnetic flux density estimated from the observed oscillation period was 0.423 T mm, which meant that the average spontaneous magnetization (M_s) was 1.84 T for the sample thickness of 0.23 mm. Several lateral lines with opposite polarity as compared with the rest of the sample indicate the existence of magnetic domains with magnetization anti-parallel to the remaining area. From these results, it was confirmed that the pulsed polarized neutron imaging can visualize the domain structure inside a surface-coated GO steel with quantitative estimation of M_s as an integrated value along the sample thickness. In addition to the study of magnetic materials, some imaging studies visualizing magnetic field distributions for commercial products, e.g., electric motors and electric transformers, have also been conducted at RADEN.[55–57]

D. Radiography and tomography[58]

RADEN aims to provide a superior experimental environment for energy-resolved neutron imaging as a top priority but also has a role for conventional imaging as mentioned above. Here, we present some demonstration results for conventional radiography and tomography using a white neutron beam. The radiography and tomography experiments were conducted using the camera-type detector consisting of a back-illuminated CCD camera and a ^{6}LiF + ZnS scintillator screen with 100 μm thickness.

As a first example, photographs and transmission images of ball bearings (a) before and (b) after packing with grease are shown in Fig. 20. The transmission images were taken with a FoV of 180 × 180 mm^2 and a L/D of 398. The exposure time was 120 s at the proton beam power of 300 kW. The distance between the sample and the scintillator screen was set to 50 mm. The internal components of the ball bearing, such as the steel balls and bearing retainer, were clearly seen through the opaque steel casing for the sample without grease, while the distribution of grease is emphasized compared to the metal parts for the sample with grease.

As a second example, Figs. 21(a) and 21(b) show the photograph and transmission image of a soybean seedling grown in silica

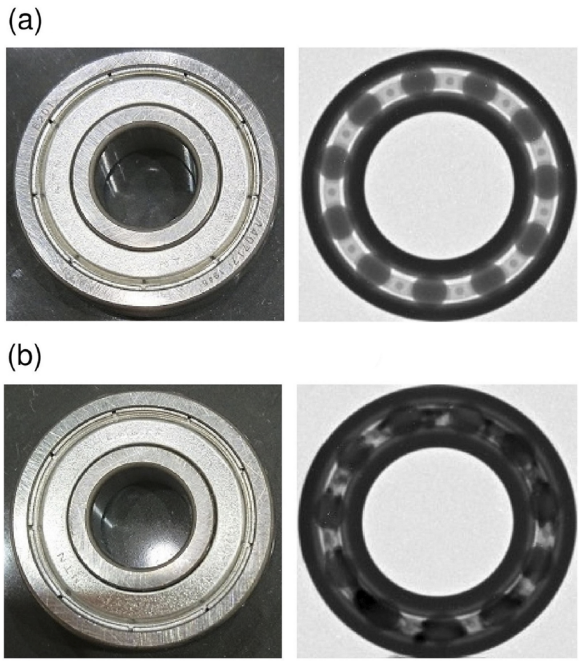

FIG. 20. Photographs and transmission images of ball bearings (a) before and (b) after packing with grease.

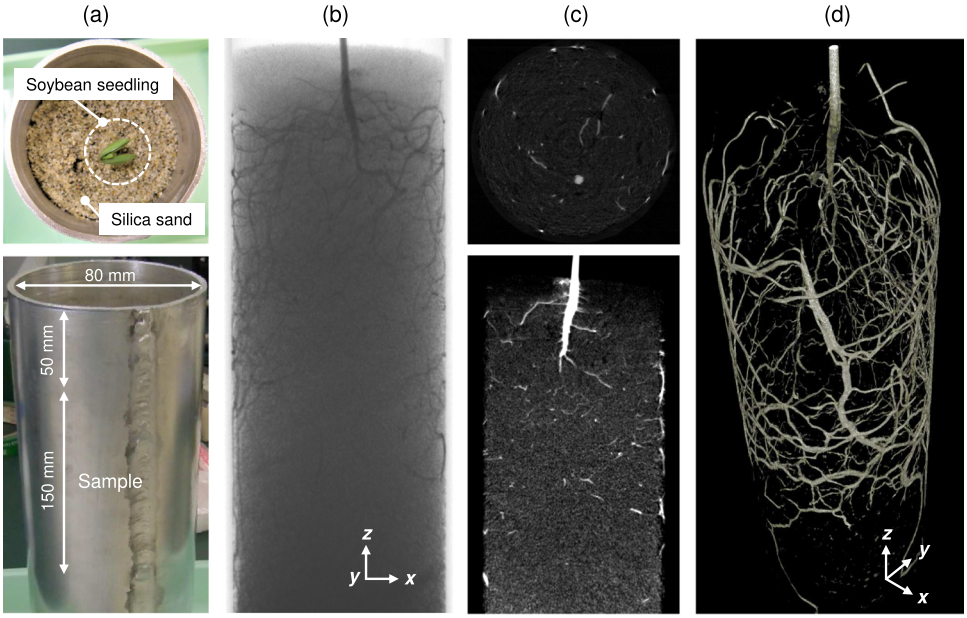

FIG. 21. (a) Photograph, (b) transmission image, (c) tomograms, and (d) three-dimensional image of the soybean seedling grown in silica sand.

sand taken with a FoV of 200 × 200 mm^2 and a L/D of 398. The exposure time was 120 s at the proton beam power of 400 kW. The distance between the sample and the scintillator screen was 80 mm. Water in the silica sand was removed before observation. The transmission image of Fig. 21(b) displays the soybean roots spreading in silica sand. In order to visualize the three-dimensional distribution of the roots, a tomography measurement was performed. Figures 21(c) and 21(d) show several tomograms and the three-dimensional distribution of the soybean roots reconstructed using the FBP algorithm, respectively. The projection images used for the reconstruction were taken by rotating the sample from 0° to 180° by 0.6° steps. As a result, the three-dimensional soybean root growth under *in situ* condition was successfully visualized after excluding the silica sand.

Furthermore, it is possible to conduct energy-selective radiography and tomography by means of ToF at RADEN. In particular, epi-thermal neutron radiography/tomography is a unique imaging technique suitable for imaging objects that contain materials with high neutron attenuation. Such application studies are ongoing in the nuclear related and the civil engineering field at RADEN.

VII. CONCLUSION

RADEN was constructed as the world's first dedicated imaging instrument at a pulsed neutron source. This instrument has been optimized to perform pulsed neutron imaging and has been used in various application fields. The results of its neutronic performance studies revealed the advantages of the short-pulsed neutron beam both in the wavelength/energy resolution and in the broadness of the available energy range, which are important for both the Bragg-edge and resonance absorption imaging techniques. Consequently, together with the newly developed detectors with ToF analysis capability and specially designed devices such as the polarization analysis apparatus, RADEN provides the most suitable environment for energy-resolved neutron imaging experiments at J-PARC. The application studies presented for each energy-resolved neutron imaging technique demonstrated the usefulness and effectiveness of this instrument to produce new information, which cannot be obtained by conventional imaging techniques. Our continuing technical developments on energy-resolved neutron imaging will be integrated into RADEN in order to support ever wider application fields and pioneer new neutron imaging methods.

ACKNOWLEDGMENT

The authors would like to gratefully acknowledge Professor M. Arai, the former division head of the MLF, and the International Advisory Committee members of RADEN for their useful advice and assistance and the continuing support of the J-PARC MLF members. Part of this work was supported by JSPS KAKENHI Grant No. 23226018 and "The Photon and Quantum Basic Research Coordinated Development Program" from MEXT, Japan. The commissioning and application studies were conducted under Instrument group and Project proposals (Nos. 2015I0022, 2016I0022, 2017I0022, 2018I0022, 2015P0701, 2016P0701, 2017C0004, and 2018C0002), and the measurement of the soybean seedling was performed by H. Takahashi, S. Nishiuchi, and M. Nakazono (Nagoya University) under the General use proposal (No. 2017B0108).

REFERENCES

[1] Y. Kiyanagi, H. Sato, T. Kamiyama, and T. Shinohara, J. Phys.: Conf. Ser. **340**, 012010 (2012).
[2] M. Strobl, I. Manke, N. Kardjilov, A. Hilger, M. Dawson, and J. Banhart, J. Phys. D: Appl. Phys. **42**, 243001 (2009).
[3] J. R. Santisteban, L. Edwards, M. E. Fizpatrick, A. Steuwer, and P. J. Withers, Appl. Phys. A: Mater. Sci. Process. **74**, s1433 (2002).

[4]H. Sato, T. Kamiyama, and Y. Kiyanagi, Mater. Trans. **52**, 1294 (2011).
[5]R. Woracek, D. Penumadu, N. Kardjilov, A. Hilger, M. Boin, J. Banhart, and I. Manke, Adv. Mater. **26**, 4069 (2014).
[6]A. Tremsin, W. Kockelmann, J. Kelleher, A. Paradowska, R. Ramadhan, and M. Fitzpatrick, J. Imaging **4**, 48 (2018).
[7]T. Kamiyama, J. Ito, H. Noda, H. Iwasa, Y. Kiyanagi, and S. Ikeda, Nucl. Instrum. Methods Phys. Res., Sect. A **542**, 258 (2005).
[8]H. Sato, T. Kamiyama, and Y. Kiyanagi, Nucl. Instrum. Methods Phys. Res., Sect. A **605**, 36 (2009).
[9]T. Kai, F. Maekawa, H. Oshita, H. Sato, T. Shinohara, M. Ooi, M. Harada, S. Uno, T. Otomo, T. Kamiyama, and Y. Kiyanagi, Phys. Procedia **43**, 111 (2013).
[10]A. S. Tremsin, T. Shinohara, T. Kai, M. Ooi, T. Kamiyama, Y. Kiyanagi, Y. Shiota, J. B. McPhate, J. V. Vallerga, O. H. W. Siegmund, and W. B. Feller, Nucl. Instrum. Methods Phys. Res., Sect. A **746**, 47 (2014).
[11]N. Kardjilov, I. Manke, M. Strobl, A. Hilger, W. Treimer, M. Meissner, T. Krist, and J. Banhart, Nat. Phys. **4**, 399 (2008).
[12]M. Strobl, N. Kardjilov, A. Hilger, E. Jericha, G. Badurek, and I. Manke, Physica B **404**, 2611 (2009).
[13]T. Shinohara, K. Sakai, M. Ohi, T. Kai, M. Harada, K. Oikawa, F. Maekawa, J. Suzuki, T. Oku, S. Takata, K. Aizawa, M. Arai, and Y. Kiyanagi, Nucl. Instrum. Methods Phys. Res., Sect. A **651**, 121 (2011).
[14]F. Pfeiffer, C. Grünzweig, O. Bunk, G. Frei, E. Lehmann, and C. David, Phys. Rev. Lett. **96**, 215505 (2006).
[15]M. Strobl, Sci. Rep. **4**, 7243 (2014).
[16]D. A. Pushin, D. Sarenac, D. S. Hussey, H. Miao, M. Arif, D. G. Cory, M. G. Huber, D. L. Jacobson, J. M. LaManna, J. D. Parker, T. Shinohara, W. Ueno, and H. Wen, Phys. Rev. A **95**, 043637 (2017).
[17]Y. Seki, T. Shinohara, J. D. Parker, W. Ueno, T. Samoto, W. Yashiro, A. Momose, Y. Otake, and Y. Kiyanagi, Europhys. Lett. **123**, 12002 (2018).
[18]D. Sarenac, D. A. Pushin, M. G. Huber, D. S. Hussey, H. Miao, M. Arif, D. G. Cory, A. D. Cronin, B. Heacock, D. L. Jacobson, J. M. LaManna, and H. Wen, Phys. Rev. Lett. **120**, 113201 (2018).
[19]Y. Kiyanagi, T. Kamiyama, H. Sato, T. Shinohara, T. Kai, K. Aizawa, M. Arai, M. Harada, K. Sakai, K. Oikawa, M. Ohi, F. Maekawa, T. Sakai, M. Matsubayashi, M. Segawa, and M. Kureta, Nucl. Instrum. Methods Phys. Res., Sect. A **651**, 16 (2011).
[20]T. Shinohara, T. Kai, K. Oikawa, M. Segawa, M. Harada, T. Nakatani, M. Ooi, K. Aizawa, H. Sato, T. Kamiyama, H. Yokota, T. Sera, K. Mochiki, and Y. Kiyanagi, J. Phys. Conf. Ser. **746**, 012007 (2016).
[21]T. Minniti, K. Watanabe, G. Burca, D. E. Pooley, and W. Kockelmann, Nucl. Instrum. Methods Phys. Res., Sect. A **888**, 184 (2018).
[22]H. Bilheux, K. Herwig, S. Keener, and L. Davis, Phys. Procedia **69**, 55 (2015).
[23]M. Strobl, "The scope of the imaging instrument project ODIN at ESS," Phys. Procedia **69**, 18 (2015).
[24]M. Furusaka, H. Sato, T. Kamiyama, M. Ohnuma, and Y. Kiyanagi, Phys. Procedia **60**, 167 (2014).
[25]K. Oikawa, F. Maekawa, M. Harada, T. Kai, S. Meigo, Y. Kasugai, M. Ooi, K. Sakai, M. Teshigawara, S. Hasegawa, M. Futakawa, Y. Ikeda, and N. Watanabe, Nucl. Instrum. Methods Phys. Res., Sect. A **589**, 310 (2008).
[26]K. Shibata, O. Iwamoto, T. Nakagawa, N. Iwamoto, A. Ichihara, S. Kunieda, S. Chiba, K. Furutaka, N. Otuka, T. Ohsawa, T. Murata, H. Matsunobu, A. Zukeran, S. Kamada, and J.-i. Katakura, J. Nucl. Sci. Technol. **48**, 1 (2011).
[27]K. Oikawa, M. Harada, and F. Maekawa, JPS Conf. Proc. **1**, 014012 (2014).
[28]P. Willendrup, E. Farhi, and K. Lefmann, Physica B **350**, E735 (2004).
[29]K. Niita, T. Sato, H. Iwase, H. Nose, H. Nakashima, and L. Sihver, Radiat. Meas. **41**, 1080 (2006).
[30]Y. Kiyanagi, T. Shinohara, T. Kai, T. Kamiyama, H. Sato, K. Kino, K. Aizawa, M. Arai, M. Harada, K. Sakai, K. Oikawa, M. Ooi, F. Maekawa, H. Iikura, T. Sakai, M. Matsubayashi, M. Segawa, and M. Kureta, Phys. Procedia **43**, 92 (2013).
[31]K. Oikawa, M. Harada, T. Shinohara, T. Kai, M. Ooi, and Y. Kiyanagi, JPS Conf. Proc. **8**, 036002 (2015).
[32]M. Segawa, K. Oikawa, T. Kai, T. Shinohara, H. Hayashida, Y. Matsumoto, J. D. Paker, T. Nakanati, K. Hiroi, Y. H. Su, and Y. Kiyanagi, JPS Conf. Proc. **22**, 011028 (2018).
[33]J. D. Parker, M. Harada, K. Hattori, S. Iwaki, S. Kabuki, Y. Kishimoto, H. Kubo, S. Kurosawa, Y. Matsuoka, K. Miuchi, T. Mizumoto, H. Nishimura, T. Oku, T. Sawano, T. Shinohara, J. Suzuki, A. Takada, T. Tanimori, and K. Ueno, Nucl. Instrum. Methods Phys. Res., Sect. A **726**, 155 (2013).
[34]S. Uno, T. Uchida, M. Sekimoto, T. Murakami, K. Miyama, M. Shoji, E. Nakano, and T. Koike, Phys. Procedia **37**, 600 (2012).
[35]S. Satoh, JPS Conf. Proc. **8**, 051001 (2015).
[36]T. Mizumoto, Y. Matsuoka, Y. Mizumura, T. Tanimori, H. Kubo, A. Takada, S. Iwaki, T. Sawano, K. Nakamura, S. Komura, S. Nakamura, T. Kishimoto, M. Oda, S. Miyamoto, T. Takemura, J. Parker, D. Tomono, S. Sonoda, K. Miuchi, and S. Kurosawa, Nucl. Instrum. Methods Phys. Res., Sect. A **800**, 40 (2015).
[37]J. D. Parker, M. Harada, H. Hayashida, K. Hiroi, T. Kai, Y. Matsumoto, T. Nakatani, K. Oikawa, M. Segawa, T. Shinohara, Y. H. Su, A. Takada, T. Takemura, T. Taniguchi, T. Tanimori, and Y. Kiyanagi, JPS Conf. Proc. **22**, 011022 (2018).
[38]J. D. Parker, M. Harada, H. Hayashida, K. Hiroi, T. Kai, Y. Matsumoto, T. Nakatani, K. Oikawa, M. Segawa, T. Shinohara, Y. H. Su, S. Y. Zhang, S. Satoh, and Y. Kiyanagi, in *2015 IEEE Nuclear Science Symposium and Medical Imaging Conference (NSS/MIC)* (IEEE, 2016), Vol. 1.
[39]T. Kai, S. Satoh, K. Hiroi, Y. H. Su, M. Segawa, J. D. Parker, Y. Matsumoto, H. Hayashida, T. Shinohara, K. Oikawa, and Y. Kiyanagi, Physica B **551**, 496 (2018).
[40]T. Nakatani, Y. Inamura, T. Ito, and K. Moriyama, in *Proceedings of NOBUGS2016* (NOBUGS, 2016), p. 76.
[41]K. Nakayoshi, Y. Yasu, E. Inoue, H. Sendai, M. Tanaka, S. Satoh, S. Muto, N. Kaneko, T. Otomo, T. Nakatani, and T. Uchida, Nucl. Instrum. Methods Phys. Res., Sect. A **600**, 173 (2009).
[42]T. Nakatani, Y. Inamura, K. Moriyama, T. Ito, S. Muto, and T. Otomo, JPS Conf. Proc. **1**, 014010 (2014).
[43]S. Harjo, T. Ito, K. Aizawa, H. Arima, J. Abe, A. Moriai, T. Iwahashi, and T. Kamiyama, Mater. Sci. Forum **681**, 443 (2011).
[44]R. B. Von Dreele, J. D. Jorgensen, and C. G. Windsor, J. Appl. Crystallogr. **15**, 581 (1982).
[45]H. Sato, T. Sato, Y. Shiota, T. Kamiyama, A. S. Tremsin, M. Ohnuma, and Y. Kiyanagi, Mater. Trans. **56**, 1147 (2015).
[46]Y. H. Su, K. Oikawa, S. Harjo, T. Shinohara, T. Kai, M. Harada, K. Hiroi, S. Y. Zang, J. D. Parker, H. Sato, Y. Shiota, Y. Kiyanagi, and Y. Tomota, Mater. Sci. Eng.:A **675**, 19 (2016).
[47]Y. H. Su, K. Oikawa, T. Shinohara, T. Kai, K. Hiroi, S. Harjo, T. Kawasaki, W. Gong, S. Y. Zhang, J. D. Parker, H. Hayashida, H. Sato, Y. Kiyanagi, and Y. Tomota, Phys. Procedia **88**, 42 (2017).
[48]M. Strobl, H. Heimonen, S. Schmidt, M. Sales, N. Kardjilov, A. Hilger, I. Manke, T. Shinohara, and J. Valsecchi, J. Phys. D: Appl. Phys. **52**, 123001 (2019).
[49]F. M. Piegsa, B. van den Brandt, P. Hautle, J. Kohlbrecher, and J. A. Konter, Phys. Rev. Lett. **102**, 145501 (2009).
[50]J. Valsecchi, R. P. Harti, M. Raventós, M. D. Siegwart, M. Morgano, P. Boillat, M. Strobl, P. Hautle, L. Holitzner, U. Filges, W. Treimer, F. M. Piegsa, and C. Grünzweig, Nat. Commun. **10**, 3788 (2019).
[51]N. Wada, T. Shinohara, H. Sato, H. Hasemi, T. Kamiyama, and Y. Kiyanagi, Phys. Procedia **69**, 427 (2015).
[52]T. Shinohara, K. Hiroi, Y. H. Su, T. Kai, T. Nakatani, K. Oikawa, M. Segawa, H. Hayashida, J. D. Parker, Y. Matsumoto, S. Y. Zhang, and Y. Kiyanagi, J. Phys.: Conf. Ser. **862**, 012025 (2017).
[53]K. Hiroi, T. Shinohara, H. Hayashida, J. D. Parker, Y. H. Su, K. Oikawa, T. Kai, and Y. Kiyanagi, Physica B **551**, 146 (2018).
[54]M. Th. Rekveldt, Z. Phys. **259**, 391 (1973).
[55]K. Hiroi, T. Shinohara, H. Hayashida, J. D. Parker, K. Oikawa, M. Harada, Y. H. Su, and T. Kai, J. Phys.: Conf. Ser. **862**, 012008 (2017).
[56]K. Hiroi, T. Shinohara, H. Hayashida, J. D. Parker, K. Oikawa, Y. H. Su, T. Kai, and Y. Kiyanagi, JPS Conf. Proc. **22**, 011030 (2018).
[57]M. Sales, M. Strobl, T. Shinohara, A. S. Tremsin, L. T. Kuhn, W. R. B. Lionheart, N. M. Desai, A. B. Dahl, and S. Schmidt, Sci. Rep. **8**, 2214 (2018).
[58]Y. Matsumoto, M. Segawa, T. Kai, T. Shinohara, T. Nakatani, K. Oikawa, K. Hiroi, Y. H. Su, H. Hayashida, J. D. Parker, S. Y. Zhang, and Y. Kiyanagi, Phys. Procedia **88**, 162 (2017).